FABRICATION AND CHARACTERIZATION OF GRAPHENE QUANTUM DOTS FOR ELECTRONIC AND OPTOELECTRONIC APPLICATIONS

LUK CHI MAN

Ph.D

The Hong Kong Polytechnic University

2015

The Hong Kong Polytechnic University

Department of Applied Physics

Fabrication and Characterization of Graphene Quantum Dots For Electronic and Optoelectronic Applications

Luk Chi Man

A thesis submitted in partial fulfillment of the requirements for the degree of Doctor of Philosophy

February 2015

Certificate of originality

I hereby declare that this thesis is my own work and that, to the best of my knowledge and belief, it reproducers no material previously published or written, nor material that has been accepted for the award of any other degree or diploma, except where due acknowledgement has been made in the text.

_____ (Signature)

Luk Chi Man (Name of candidate)

Abstract

Graphene quantum dots (GQDs) are nano-scale fragments of one or few-layer graphene, composed of regular hexagonal lattice sp^2 carbon atoms edged with heteroatomic functional groups. They attract particular research interest because of their unique properties such as UV-visible absorption, tunable luminescence, biocompatibility, low toxicity, chemical stability and hot carrier generation. In this work, we investigate the synthesis and characterization of GQDs. The GQDs were synthesized by microwave-assisted hydrothermal technique. It is found that the size of the GQDs varied with the reaction time and pressure. The structural and optical properties of the GQDs were characterized by transmission electron microscopy (TEM), Fourier Transform Infrared (FT-IR) spectroscopy, UV-visible absorbance spectroscopy and photoluminescence (PL).

The high resolution transmission electron microscopy (HR-TEM) revealed that the GQDs consist of graphitic structure. As identified by electron energy loss spectroscopy (EELS), the GQDs contain various functional groups on the GQD surface, making the GQDs water soluble. Room temperature PL showed excitation wavelength dependent emission. The tunable luminescence was attributed to the emissive traps resulted from the functional groups at the surface of GQD.

Because of strong PL emissions of GQDs, we fabricated GQD-agar composite and utilized as a light conversion material in a commercial blue LED. The luminous efficiency of the composite-coated LED is 42.2 lm W^{-1}. The colour rendering index (CRI) and correlated colour temperature (CCT) of the composite coated LED were determined to be 72.0 and 5532 K, corresponding to cool white

colour. The light conversion efficiency of the WLED is 61.1 % under 20 mA of forward current.

GQDs-polyaniline (PANI-GQD) composite was synthesized by chemical oxidation polymerization. The PL spectra were found to be tuned by varying the mole concentration of PANI and sizes of the GQDs. The Au/PANI-GQD/ITO sandwich device was fabricated to study the electrical transport of the composite film. Electrical hysteresis was observed in response to the applied voltage. Both the tunable PL and electrical hysteresis behavior were attributed to the surface states of the GQDs.

The two-photon luminescence of nitrogen doped GQDs (N-GQDs) has been demonstrated. The strongest PL was located at 517 nm when the excitation wavelength was 800 nm. The power-dependent emission of the N-GQDs also showed the quadratic relationship between the emission intensity and laser power. The intensity of two-photon emission of the N-GQDs was found to be altered with various N/C atomic ratios. It showed that N doping play an important role in two-photon luminescence.

The emissive properties of both undoped and N doped GQDs were characterized at single particle level. The relative particle population of red and NIR emitting GQDs were compared. It was shown that N-GQDs exhibited larger proportion of particles with near infrared (NIR) emission compared with undoped GQDs. Both undoped and N-GQDs showed size dependent photophysical properties. Doping of GQDs leaded to significant changes in the NIR emissive properties.

List of publications

1. C. M. Luk, B. L. Chen, K. S. Teng, L. B. Tang and S. P. Lau, Optically and Electrically Tunable Graphene Quantum Dots-Polyaniline Composite Films, Journal Of Materials Chemistry C, 2 (2014), 4526.

2. C. M. Luk, M. K. Tsang, C. F. Chan and S. P. Lau, Two-Photon Fluorescence in N-Doped Graphene Quantum Dots, International Journal of Chemical, Nuclear, Metallurgical and Materials Engineering (2014) Vol:8 No:12, 143.

3. C. M. Luk, L. B. Tang, W. F. Zhang, S. F. Yu, K. S. Teng and S. P. Lau, An Efficient and Stable fluorescent Graphene Quantum Dot-Agar Composite As a Converting Material in White Light Emitting Diodes, Journal of Materials Chemistry, 22 (2012) 22378.

4. S. K. Das, C. M. Luk, W. E. Martin, L. Tang, D. Y. Kim, S. P. Lau and C. I. Richards, Size and Dopant Dependent Single Particle Fluorescence Properties of Graphene Quantum Dots, *The Journal of Physical Chemistry C* (2015), 119 (31), 17988-17994.

5. C.Y. Chen, H. Qiao, S. H. Lin, C. M. Luk, Y. Liu, Z. Q. Xu, J. C. Song, Y. Z. Xue, D. L. Li, J. Yuan, W. Z. Yu, C. X. Pan, S. P. Lau and Q. L. Bao, Highly responsive MoS_2 photodetectors enhanced by graphene quantum dots, Scientific Reports 5 (2015), 11830.

6. S. K. Lai, C. M. Luk, L. B. Tang, K. S. Teng and S. P. Lau, Photoresponse of Polyaniline-functionalized Graphene Quantum Dots, Nanoscale, 7 (2015), 5338-5343.

7. S. K. Lai, L. B. Tang, Y. Y. Hui, C. M. Luk and S. P. Lau, Deep Ultraviolet and to Near-Infrared Photoresponse from Glucose-derived Graphene Oxide, Journal Of Materials Chemistry C, 2 (2014), 6971-6977.

8. Y. H. Zhu, J. Jiang, Y. K. Xiao, C. M. Luk and W. E. Lai, Electropulsing-induced Microstructure Evolution and Its Effect on Electrical Conductivity of $(Bi_{0.25}Sb_{0.75})_2Te_3$ Thin Films, Scripta Materialia, 69 (2013), 219

9. L. B. Tang, R. B. Ji, X. K. Cao, J. Y. Lin, H. X. Jiang, X. M. Li, K. S. Teng, C. M. Luk, S. J. Zeng, J. H. Hao, and S. P. Lau, Deep Ultraviolet Photoluminescence of Water-Soluble Self-Passivated Graphene Quantum Dots, ACS Nano, 6 (2012), 5102.

Acknowledgment

I would like to thank my supervisor Prof. S. P. Lau for his professional and invaluable advices in my PhD study. His broad view, deep insight and opinions helped me a lot through difficulties in my research and study. I also wish to thank Prof. S. F. Yu for the discussion of experiments during my study and Dr. W. Lu, Dr. Hardy Lui, as well as Mr. C. S. Lo for their assistant of experimental measurements.

I would greatly appreciate the collaboration with Prof. C. I. Richards from Department of Chemistry in University of Kentucky for single particle measurement, Dr. K. S. Teng from College of Engineering in Swansea University for X-ray photoelectron spectroscopy measurement, and Mr. C. F. Chan from Department of Chemistry in The City University of Hong Kong for measurement of two-photon fluorescence. They provided me useful help, discussion and assistance in experiments during the collaboration.

My special thanks are also given to my colleagues for providing me with help and support throughout my study. They include Dr. B. L. Chen, Dr. L. B. Tang, Dr. Y. Y. Hui, Dr. N. Y. Chan, Dr. N. Wang, Mr. J. S. Qian, Mr. W. F. Zhang, Miss S. M. Ng and Miss F. R. Tan. My study in PolyU has been full of brilliant memories and warm friendships with all of them.

Last but not least, I truly appreciate the continued encouragement, endless supports and understanding from my parents and my wife Miss Yeda Tsoi during my research study. They have been inspiring me at every moment.

Table of contents

List of figures

List of tables

Chapter 1 Introduction

1.1 *Background and motivation*

Nanostructures with spatial dimension comparable to the de Broglie wavelength of charge carrier are readily regulated with nanoscale precision. Quantum confinement in a critical dimension threshold converts the continuous optical spectrum of a bulk semiconductor into a size-dependent and atomic-like spectrum, determining a widening of the forbidden band gap and energy level discretization at the band edges. In the past few decades, novel semiconductor nanostructures have been realized for a number of technologically valuable applications, including optical communications, display technologies, solar energy harvesting and information processing. In order to explore their novel properties and potential applications, the fabrication of nanostructures become very significant. Because of quantum phenomena arisen from zero dimensional (0D) confinement, it leads to a sharp rise in number of research groups involved in semiconductor quantum dots (QDs). The majority of previous studies mainly focused on the fundamental electronic and optical properties of QDs and developing new fabrication methods. Among the various QDs, II-IV semiconductors, for instance, CdS, CdSe, and ZnS are the famous class of the QDs to date. They provide superior carrier mobility, light absorption and thermal stability. However, it is difficult to fabricate by low-cost technique. The crystallization of inorganic semiconductor QDs generally requires high temperature treatment, which oblige trade-offs between the device performance, compatibility and fabrication cost. Furthermore, the use of toxic precursors and development of heavy metal-based QDs lead to environmental obstruction. As a

new kind of QDs, graphene quantum dots (GQDs) have emerged and ignited tremendous research interest. Owing to the pronounced edge effect and quantum confinement, GQDs presume a variety of novel physical and chemical properties. In order to convert two-dimensional (2D) graphene to 0D GQDs, some chemical techniques including oxidation of graphene, reduced graphene oxide (r-GO) and doping r-GO can reach fluorescent graphene-based nanosystems. However, the large size of graphene limits their performance in nanodevice applications.

In this thesis, we fabricated GQDs using microwave-assisted hydrothermal technique with glucose as carbon source. The structures and optical properties of the GQDs were found to be dependent on the growth condition such as growing time, reaction pressure and temperature. Because of their stable and tunable luminescence, we prepared a GQD-polymer composite by using saccharide such as agar which is commonly used as a gel-forming agent. The composite was applied as a color converting material in blue light-emitting diode (LED) to achieve white light emission. No luminescence quenching was found on the composite. The light conversion efficiency of the white LED was stable for over 100 hours of continuous operation.

The phenomena of memory effect and electrical bi-stability of nanoparticles have been widely studied in past decades. The mechanism of conductance switching is generally attributed to electrically induced charge transfer, causing a sudden change in conductivity of materials. Depending on the various nanostructures, the switching behavior will be different. Therefore it is of high interest to study the electrically bi-stability related to low dimensional system. We have fabricated composite films with mixture of the GQDs and conducting polymer to

investigate optical and charge transport properties. The photoluminescence (PL) of the composite is tunable by changing mole concentration of the polymer. A sandwich device is fabricated to study the transport properties of the composite. A stable hysteresis loop is observed in response to the applied voltage and is changed with mole concentration of the polymer as well. Both the tunable PL and hysteresis behavior are attributed to surface states of the GQDs.

Doping carbon-based nanomaterials with heteroatoms can effectively alter their electronic properties, surface and chemical reactivity. Among various dopants, nitrogen (N) atom has been generally used for chemical doping of carbon nanomaterials such as N-doped graphene and N-doped carbon nanotubes. Doping of carbon nanomaterials have been shown to alter drastically their electrical characteristics. Similarly, doping GQDs with chemically bonded N atoms is able to open up a realm of electronic possibilities and provided more active optical sites, resulting in new phenomena and unique properties. Experiments have reported that the luminescence of N-GQDs can be tuned according to the dopant materials used. High N/C atomic ratio and quantum yield can be detected. Therefore, we have prepared N-GQDs through microwave-assisted hydrothermal technique in the presence of ammonia where pyridine-like and pyrrolic N atoms were present. The PL measurement shows that the N-GQDs exhibit excitation-dependent emission. Surprisingly, the N-GQDs show two-photon tunable luminescence with near infrared excitation. These results open up an opportunity for bioimaging and sensing.

The ensemble photophysical properties of GQDs are dependent on the fabrication methods, surface passivation and chemical treatment. Generally the

fluorescence spectrum of GQDs exhibits mutichromophoric behaviors. While the exact mechanism is still not fully understood, a detailed investigation is necessary to determine whether the multiple emissions are contained within single GQD or from separate particles. Hence, single particle measurement allows the characterization of fluorescence properties of GQDs at single particle level. We characterized the single-particle fluorescence of both undoped and N doped GQDs with various sizes and dopant concentrations. The N-GQDs show a large proportion of particles with near infrared (NIR) emission. Doping of GQDs resulted in significant changes in the emissive properties of NIR emitting GQDs including photostability and single particle fluorescence intermittency.

1.2 *Scope of this project*

In this project, we synthesized GQDs and GQDs-based composite materials. Their structural, optical and electrical properties are characterized. The GQDs were used as color converting material on the blue LED and white light emission was observed. The performance of the white LED was investigated. The GQDs-based composite device was demonstrated. The transport properties of the composite were also studied. Furthermore, the doped GQDs were prepared and their optical properties were examined.

In chapter 2, the brief information and development of the GQDs are described.

In chapter 3, the experimental details are described. They include structural and optical characterizations such as, transmission electron microscope (TEM), UV-Vis absorption measurement and photoluminescence (PL) measurement. The experimental setup for the growth of the GQDs is also explained.

In chapter 4, the synthesis and characterization of GQDs are described. Also, the fabrications of the GQDs-agar composite and white LED are discussed. It is suggested that the GQDs based light emitter is possible.

In chapter 5, the synthesis and characterization of GQD-PANI composite are studied. The fabrication of GQD-PANI sandwich device and transport properties of the composite are discussed. The GQD-PANI composite may find application in photonic device.

In chapter 6, the synthesis and characterization of N-doped GQDs are discussed. The properties of two-photon luminescence are studied. The N-doped GQDs may open an opportunity for bioimaging and sensing applications.

In chapter 7, the NIR emissive properties of N-GQDs are analyzed at single particle level. It is found that doping concentration of GQDs leads to significant change in near infrared emission and single particle fluorescence intermittency.

In chapter 8, the work in this thesis is concluded and future work is discussed.

Chapter 2 Graphene Quantum Dots

2.1 *Review*

Nowadays, the development of nanotechnology in both optical and electronic devices has been emerging. Materials in nanoscale exhibit unique and fascinating physical and mechanical properties as compared to the bulk. The quantum size effect and increase of surface area-to-volume ratio modify electron distribution resulting in size-dependent properties such as band gap and energy relaxation dynamics. In order to explore their novel properties and potential applications, the fabrication of nanostructures become very significant.

Among those nanosystems, zero-dimensional (0D) materials have been considered as a powerful class of materials due to their unusual optoelectronic properties resulting from the size quantization effect when the nanoparticles radius is below the exciton Bohr radius and have typical diameters of 2 – 20 nm [1]. Such materials, also named quantum dots, are implied as artificial atoms that confine an electron or a hole in all three dimensions and which is sufficiently small to cause quantization of the energy levels analogous to atoms. Many 0D materials such as metal-chalcogenide (ME) possess size-tuned optical response and multiple carrier generation. The electronic structure can also be tuned by varying their size. Since the discovery of graphene in 2004 by Geim and Novoselov [2], graphene has emerged as one of the most active research field. The fascinating structures and properties of graphene have been well demonstrated [3-5]. Because graphene has no band gap, the possibility for the

observation of its luminescence is rare, which hinders its optoelectronics application [6, 7]. In principle, the band gap of graphene can be opened by varying their sizes [8]. Consequently, graphene quantum dots (GQDs), as a new kind of 0D material, have emerged and ignited tremendous research interest due to the pronounced quantum confinement and edge effects. GQDs also show excellent solubility, chemical inertia, stable photoluminescence, better surface grafting, thus making them promising in optoelectronic devices, sensors and bioimaging [9–18].

Another two examples of 0D carbon-based fluorescent nanomaterials, nanodiamonds [19, 20] and carbon dots (CDs) [21, 22] have also been investigated in recent years. For clarification purposes, extraordinary consideration is needed to distinguish these three types of nanomaterials. In general, nanodiamonds consist of about 98% carbon with residual hydrogen, oxygen, and nitrogen, possess a sp^3 hybridized core, and have small amounts of graphitic carbon on the surface. They also emit from point defects, particularly the negatively charged nitrogen vacancy site [23]. The CDs have greater sp^2 character, which is symbolic of nanocrystalline graphite, and contain lower amounts of carbon with higher oxygen content. Both CDs and GQDs are superior in terms of chemical inertness, tunable luminescence emission, low cytotoxicity and excellent biocompatibility, long term resistance to photobleaching. [24,25] Besides, from the views of environmental and biological hazards of QDs, they have high priority over toxic metal-based QDs currently in use, showing great potential as low-toxicity as well as ecofriendly alternatives which have the advantageous characteristics of QDs. Some differences between GQDs and CDs must be issued. The CDs are either amorphous or crystalline [23], while GQDs

are generally either prepared from graphene-based starting materials or the rigid synthetic chemistry of graphene-like smaller polycyclic aromatic hydrocarbon molecules (PAHs), thus they clearly possess graphene lattices inside the dots regardless of the dot size [9,26]. Moreover, due to the size effects, luminescent CDs comprise discrete, quasi-spherical carbon nanoparticles with sizes below 10 nm [23, 27, 28]. Meanwhile, the GQDs are defined as the graphene sheets with lateral dimensions less than 100 nm in single-, double- and few- (3 to <10) layers [9, 28, 29]

2.2 *Synthesis methods*

Fabulous effort has been made to develop fabrication technique of GQDs. Generally, approaches for synthesizing GQDs can be classified into two groups, namely top-down and bottom-up methods. The top-down methods include arc discharge [1], electron beam lithography [29], acidic exfoliation [30, 31], and electrochemical oxidation [32, 33]. In those approaches, the GQDs are derived from cleavage of carbonaceous materials, and usually contain oxygen-related functional groups at the edges, thus facilitating their solubility, functionalization and passivation. In addition, the top-down route is beneficial to abundant raw materials and large scale production. However, these methods suffer from some disadvantages, such as low yield, damage on the aromatic carbon network and requirement of special treatment [11, 34].

Conversely, the bottom-up methods consist of solution chemistry [35], combustion oxidation [36], supported synthetic [37], cage-opening of fullerene [38] and microwave methods [39], which provide size, shape and properties control of GQDs. These methods, however, involve complicated preparation

procedures and the special organic precursors which are difficult to obtain.

2.3 *Structure*

The sizes of GQDs are relevant to the fabrication method, but independent on the starting materials. In general, the average sizes of GQDs are mostly below 10 nm. Similar to size, the height of GQDs depends on the preparation method as well. With increasing the size, the height of GQDs increases accordingly through the same preparation method. Nevertheless, if the preparation method is different, the height of GQDs do not mainly related to their sizes. For example, GQDs with larger size maybe thinner than small sized one [40]. Regardless the methods used, most of GQDs consist of no more than 10 layers [11, 33, 41, 42].

The crystalline structure of GQDs strongly depends on their oxidation degree. It has been shown that the hydroxyl, epoxy, carbonyl and carboxylic acid groups attached at the GQD surface can increase the interlayer spacing of GQDs. Both (002) spacing and (100) in-plane lattice spacing of GQDs have been widely reported (Fig. 2.1). The interlayer spacing can also differ according to the fabrication approach. GQDs prepared by electrochemical cutting from graphene sheet showed an interlayer spacing of ~ 0.34 nm, comparable with that of bulk graphite (0.334 nm) [32-34, 43]. On the other hand, GQDs derived from carbon fibers obtain larger interlayer spacing of 0.403 nm, which can be attributed to the oxygen-related groups induced in the exfoliation and oxidation of carbon fibers [31].

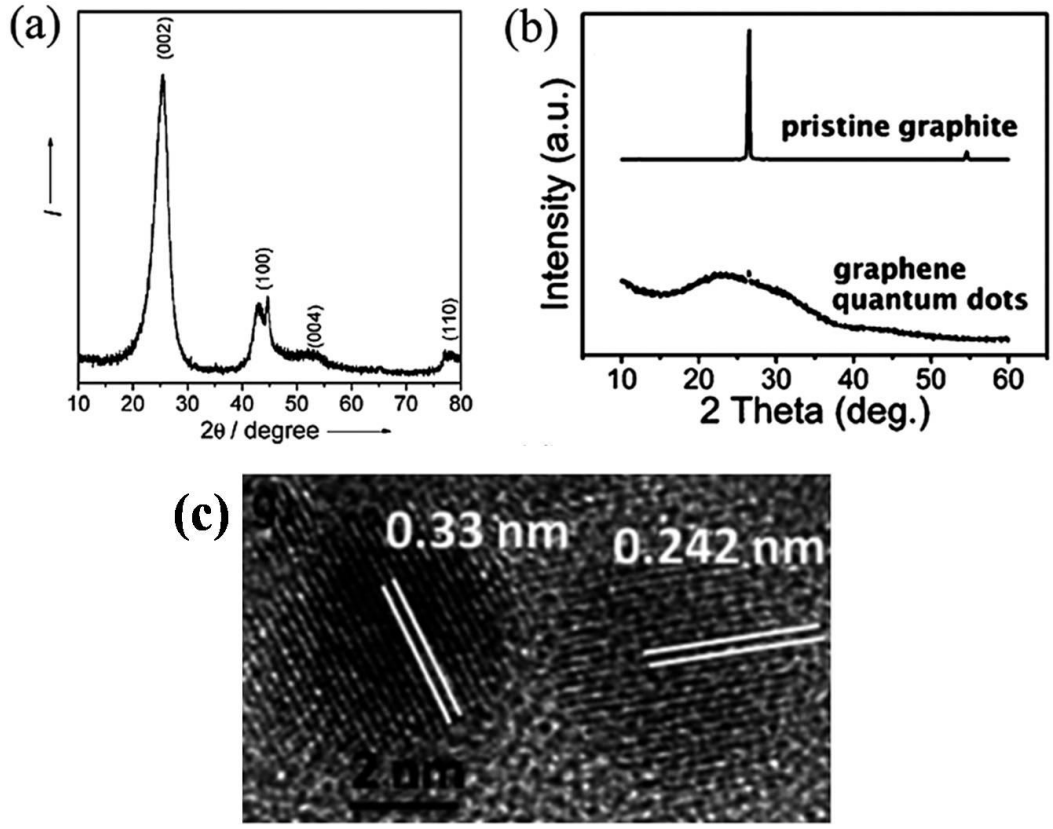

Figure 2.1 (a) Wide-angle X-ray diffraction (XRD) spectrum of the GQDs prepared by using unsubstituted HBC [26]. (b) XRD pattern of the pristine graphene and GQDs prepared via electrochemical method [33]. (c) Fringe patterns og GQDs [44].

2.4 *Optical properties*

2.4.1 *Absorption*

Typically, GQDs exhibit strong optical absorption in the ultraviolet region with a tail extending to the visible range. Two absorption peaks of GQDs are mainly observed. The π –π* transition peak is located at the wavelength between 200 and 270 nm, while the n – π* transition peak at the wavelength longer than 260 nm [33, 41, 45]. The GQDs reveal size dependent optical absorption owing to quantum confinement. The absorption peak is red-shifted with increasing the size

from 1-4 nm to 7-11 nm for carbon fibers derived GQDs [31]. However, for the glucose-derived GQDs, the absorption peaks are independent of the GQD size [11]. Hence, GQDs via various preparation methods show different absorption behaviors.

2.4.2 *Photoluminescence*

Photoluminescence (PL) is the most fascinating features of GQDs. With different sizes, the PL of GQDs can be tuned from visible to near-infrared region. Yet, the mechanism of PL for GQDs still remains questioning. The luminescence of GQDs has been hesitantly proposed to be arisen from carbon exciton, emission traps, quantum confinement, aromatic structures and oxygen-containing groups [46-52]. In addition, GQDs prepared by various approaches can emit PL with different colors, as shown in Table 2.1, including DUV, yellow, blue and green. Their PL mechanism may derive from intrinsic state and defect state emission. The former comes from either quantum size effect or recombination of localized electron-hole pairs, while the latter from defect. Different methods exhibit distinct PL mechanism, which leads to different dependences of their PL on size and excitation wavelength.

Methods	Starting materials	Emission color	Excitation	References
Acidic oxidation	GO	Blue	UV	[28]
Hydrothermal	GO	Green	UV	[10]
Electrochemistry	Graphite rod	Yellow	UV	[33]
Microwave-hydrothermal	GO	Blue	DUV	[42]
Ultrasonic treatment	Graphene	Blue	UV	[12]
Precursor pyrolysis	Glucose	DUV, blue	DUV	[11]

Table 2.1 A brief summary of the PL emission of GQDs via different methods.

Quantum confinement takes effect when the quantum dots are smaller than their exciton Bohr radius [53-55]. It consequently gives rise to size-dependent optical properties. As the particles get smaller, the luminescence energy is shifted to higher energy. Peng et al. reported their GQDs with different sizes of 1-4 nm, 4-8 nm and 7-11 nm by changing the reaction temperature. The PL emission was red-shifted as the GQD sizes were increased [31]. However, size-independent PL of GQDs was also observed from previous research works [11]. This can be ascribed to the fact that the PL mechanism of GQDs is intricate. Apart from quantum effect, other explanations such as zigzag sites, internal structure, composition and defect states also play important roles. Consequently, the size of GQDs performs a role, but not the sole determinant, in deciding the PL behaviors.

The excitation wavelength dependence of the emission wavelength is also common observation in GQDs as shown in Fig. 2.2. It is significant because such multi-color luminescence under various excitation wavelengths is important for certain practical applications [13]. The PL peak is generally red-shifted as the excitation wavelength is changed from UV to visible region [16, 26, 30, 31, 56]. The excitation dependent luminescence may result from optical selection of emissive sites [40, 57]. Those emission sites are come from, for example, hydroxyl, epoxy, carbonyl and carboxylic acid groups, which can lead to formation of surface states on GQDs [11]. Since the functional groups have various energy levels between the π and π^* states of C=C, it results in a series of emission traps. When a certain wavelength used to irradiate the GQDs, the corresponding emissive trap will dominate the emission. Nevertheless, the excitation-independent behavior has been also observed. This is mostly explained by the high uniformity both in size and surface state of those sp^2 clusters in GQDs [34].

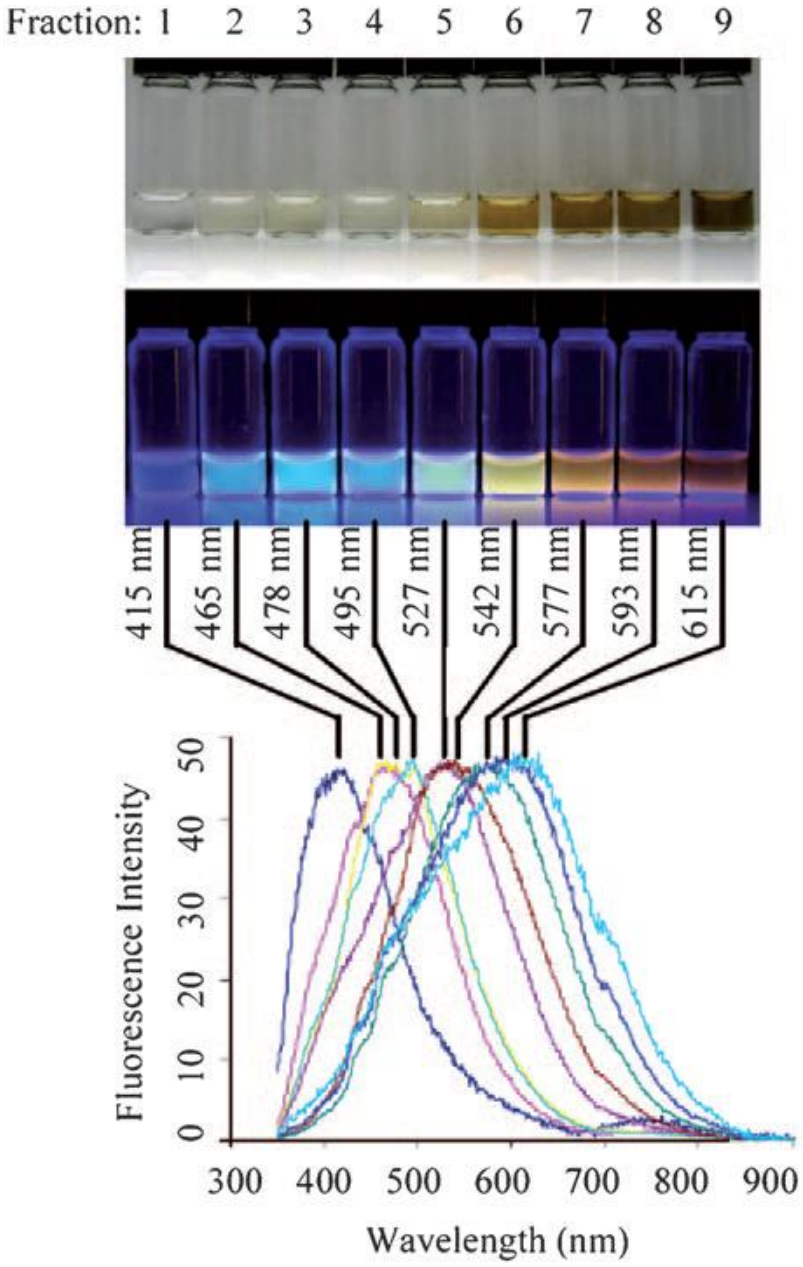

Figure 2.2 Excitation dependent PL spectrum of the GQDs prepared from candle soot [36].

2.5 *Surface functionalization*

Chemical modification using molecules with either electron-donating or-accepting ability can affect electronic characteristics of GQDs. The electron donating groups typically raises the HOMO levels, and electron withdrawing

groups lowers the LUMO levels of GQDs [58]. Tetsuka et al. demonstrated amino-functionalized GQDs via amino-hydrothermal method [59]. The degree of amine functionalization could be controlled by changing the concentration of ammonia and reaction temperature of the treatment. Multiple PL of their GQDs could be clearly observed under single UV excitation. The origin of optical tunability was explained by reaction between the delocialized π orbital and the molecular orbital in $–NH_2$ amino group. On the other hand, the electrochemically synthesized GQDs were reduced by using hydrazine hydrate, at which the hydrazine groups were attached at the edge of GQDs. When the reducing agent was changed to $NaBH_4$, the luminescence also changed [33].

The PL shift behavior of the GQDs by functionalization was studied using density functional theory (DFT) calculations [60]. The alkyl amine functional group was simplified to be an amino group ($-NH_2$) at the sp^2 clusters, which consists of 13 aromatic rings (Figure 2.3 (a)). Figure 2.3 (b) depicts the evolution of the calculated band gap of the GQDs as a function of the number of attached $-NH_2$ groups. The band gap of the GQDs decreases to 2.254 eV when a GQD is functionalized by one amino group (GQD-$(NH_2)_1$) and it gradually decreases by increasing the number of $-NH_2$ groups. When more $-NH_2$ groups are attached, the average charge of the attached $-NH_2$ groups has negative values and the band gaps of the GQD-$(NH_2)_n$ are saturated. In Figure 2.3 (c), the highest occupied molecular orbital (HOMO) for a GQD and the lowest occupied molecular orbital (LUMO) for NH_2 are observed in the HOMO isosurface for GQD-$(NH_2)_1$. According to the increased number of attached $-NH_2$ groups, more electrons diffuse from the HOMO state to the LUMO state, and consequently from a GQD to NH_2. This electron transfer from a GQD to $-NH_2$ groups compensates the

electron donation from the -NH_2 groups to the GQD. This compensation leads to minor change of the band gap of the GQD, with increasing number of attached -NH_2 groups.

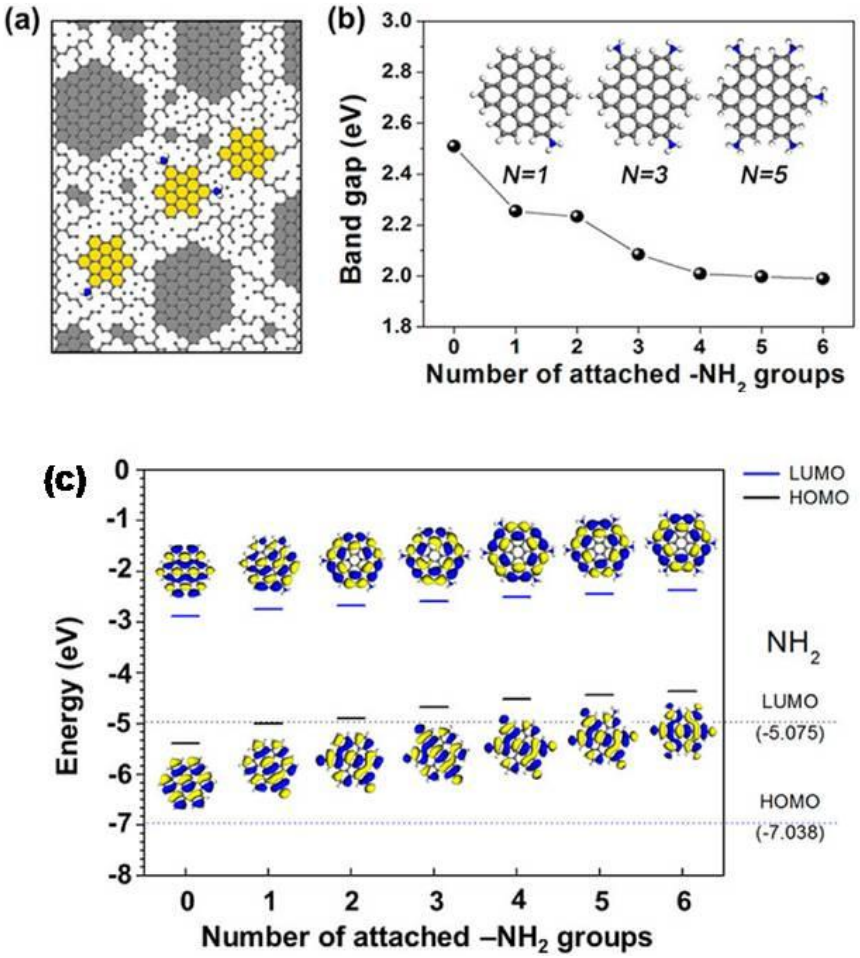

Figure 2.3 (a) Schematics of isolated sp^2 clusters with amino functional groups within the sp3 carbon matrix including defects. (b) band gap change of GQD-$(NH_2)_n$ as function of the number of attached -NH_2 groups (inset images are optimized configuration of GQD-$(NH_2)_n$. (c) HOMO and LUMO energy levels of GQDs-$(NH_2)_n$. The dotted lines denote the HOMO and LUMO energy level of NH_2 [60].

2.6 *Chemical doping*

Doping carbon nanomaterials with heteroatoms can alter the intrinsic properties including electrical properties and local chemical reactivity [61-64]. Some elements such as sulfur (S) [65], nitrogen (N) [66] and chlorine (Cl) [67] have been widely used for chemical doping of GQDs. Generally, doping GQDs with chemically bonded heteroatoms can induce new phenomena and unique properties. For example, the electrochemically prepared N-doped GQDs were found to emit blue luminescence as a result of strong electron affinity of N atom in N-GQDs, unlike the green luminescent N-free counterparts [43]. Apart from single doping, co-doping of GQDs is also reported. S, N co-doped GQDs were prepared via hydrothermal synthesis using citric acid as carbon source. Urea and thiourea were used N and S dopant, respectively. The co-doped GQDs showed high quantum yield (71%) and excitation independent emission under excitation of 340-400 nm [62].

Chapter 3 Experimental and Characterization Methods

3.1 Microwave-assisted technique

As a convenient and rapid heating source, microwave-assisted method has attract a considerable amount of attention due to its successful application in organic/inorganic synthesis, polymer chemistry, nanotechnology and biochemical processes [68, 69]. In many circumstances, the use of microwave heating has been shown to dramatically reduce reaction time, improve the product yield and enhance the material purity compared to conventionally processed experiments [70-72].

In a typical systhesis of nanocrystal, suitable molecular precursors such as organometallic compounds and metal-ligand complexes bearing the atomic elements necessary to build up the nanocrystal lattice are induced to react or decompose in a solution that contains specific functional organic species (coordinating solvents, ligands and/or surfactants) or additives (e.g., preformed crystalline seeds, metal nanoparticle catalysts) under controlled atmosphere and selected temperature and pressure conditions. Once the synthesis is initiated, highly reactive intermediate species are generated, commonly referred to as the ‘monomers’, which induce the nucleation of nanocrystals once a critical supersaturation threshold is surpassed, and sustain their subsequent enlargement.

The nanocrystal syntheses based on microwave heating can be roughly categorized in two broad classes. The first class is ambient-pressure synthesis. The reaction may be taken place in a domestic microwave oven, in which remote

temperature and pressure control, as well as stirring of the solution may be difficult to implement. This set-up configuration is most feasible only in those cases in which the reaction initiation does not require precise thermal conditions and can be safely performed under air. The second category of syntheses involves high-pressure reactions. These are carried in tightly sealed closed vessels, such as stainless steel autoclaves that may be heated either in ovens or via inner resistive heating systems. Temperatures as high as 250–300℃ and pressure of the order of 100 to 350 atm can be reached.

In this work, the graphene quantum dots (GQDs) were prepared by microwave-assisted hydrothermal method. The glucose (Sigma-Aldrich, > 99.5%) was dissolved in deionized water with the concentration of ~11 wt%. The solutions were tapped to the glass bottle with tightened cover. Two kinds of microwave treatments were applied during the synthesis process. In chapter 5, the glass bottle was heated with a domestic microwave oven (Galanz P70B17L-T1) at a power of 595 W for a specific time (1, 3, 5, 7 and 9 min). In our early studies, the use of domestic microwave oven has been shown to be an efficient method to produce controllable GQD solutions. However, it is unable to control the reaction temperature and pressure in the process. In addition, vapor explosion could occur if the glass bottle is defective. Hence, from chapter 6 to 8, the synthesis of GQDs was performed on a research grade microwave reactor (CEM Discover SP) with tunable microwave power, temperature and pressure. The fabrication was performed at 300 W with a fixed period of 5 minutes. The reaction pressures can be adjusted from 165 to 350 psi. The reaction temperature was kept constant at 180 ℃. In the process of microwave heating, the solution colour changed from

transparent to pale yellow as a result of GQDs formation. The glass bottle was cooled to room temperature under atmosphere condition without further purification. No obvious structural and optical differences can be found between the GQDs prepared by the two types of microwave apparatus. Detailed characterizations of the GQDs are described in chapter 4. Fig. 3.1 shows the schematic diagram of the fabrication of the GQDs. For N doped GQDs, the synthesis process was similar to that of undoped GQDs, except the ammonia solution (25%) was used as solvent.

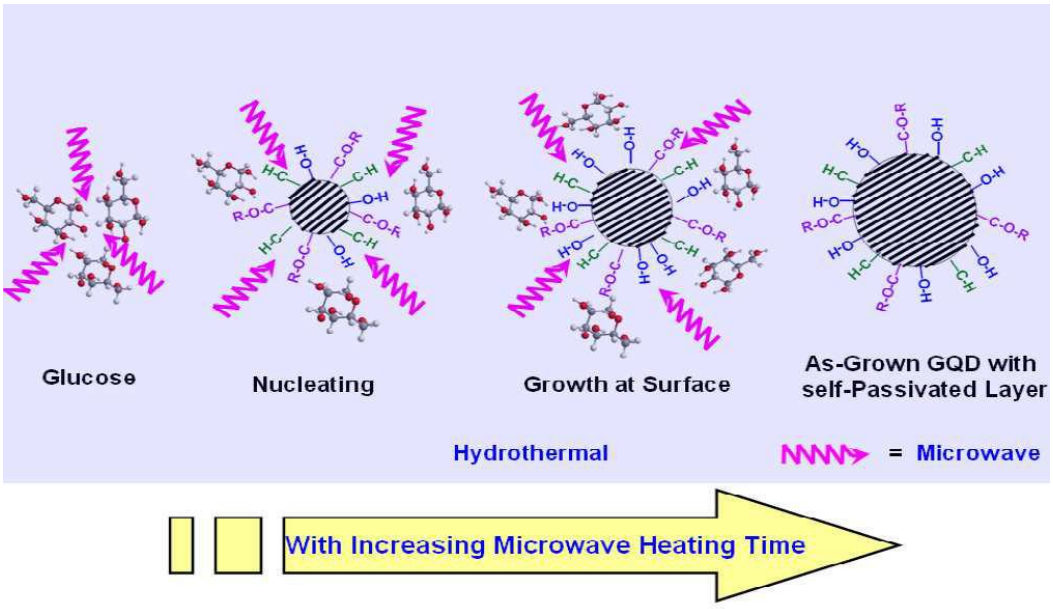

Figure 3.1 Prepartion of the GQDs by microwave-assisted hydrothermal method [11].

3.2 *Characterization methodology*

3.2.1 *Transmission electron microscopy (TEM)*

Transmission electron microscopy (TEM) is one of the precise techniques for characterization of nanostructures. It generally provides information on size, shape and arrangement of atoms within the sample. TEM consists of an electron

gun, objective lens and condenser lens. High-speed electrons emit from the electron gun when applying extremely high accelerating voltage. The condenser-lens system is used to adjust the electron illumination uniformly on the specimen. After passing through the condenser lens, a first image is formed by objective lens, followed by further magnification from intermediate and projector lenses. An entire image is then formed on the fluorescent screen. In this work, the detailed study of GQDs was performed by using JEOL JEM-2100F Electron Scanning microscope operating at 200 kV.

3.2.2 *Electron energy loss spectroscopy (EELS)*

The electron energy loss spectroscopy (EELS) of the GQDs was measured by the same TEM system simultaneously. The GQDs were irradiated to an electron beam with a known, narrow range of kinetic energies. Some of the electrons will undergo inelastic scattering, resulting in energy loss and randomly deflected electron path. The amount of energy loss can be measured via an electron spectrometer and interpreted in terms of what caused the energy loss. Inelastic interactions include, for example, phonon excitations, inner-shell ionizations and inter band transition. The inner-shell ionizations are particularly useful for detecting the elemental components of a material. For example, a number of electrons coming through the specimen are found to have 285 eV less energy than they had when they entered the material. This is approximately the amount of energy needed to remove an inner-shell electron from a carbon atom. Then we can conclude that there is a significant amount of carbon present in the sample. From a wide range of EELS spectrum, we can determine detailed information of the material including atomic composition, chemical bonding, surface properties

and band structural electronic properties.

3.2.3 *X-ray photoelectron spectroscopy (XPS)*

X-ray photoelectron spectroscopy (XPS) is a surface-sensitive quantitative technique that measures the elemental composition, chemical state and electronic state of the elements that exist within a material. XPS spectra can be obtained by irradiating a material with a beam of X-rays while simultaneously measuring the kinetic energy and number of electrons that escape from surface (0-10 nm at the top) of the material being analyzed. In our work, the XPS experiment was performed using an Al Kα source with energy of 1486.6 eV at room temperature (VG ESCAlab MKII). Since the energy of an X-ray with particular wavelength is known, and the emitted electrons kinetic energy is measured, the electron binding energy of each of the emitted electrons can be determined by using an equation [73]:

$$E_{binding} = E_{photon} - (E_{kinetic} + \emptyset) \qquad \text{(Eq. 3.1)}$$

where $E_{binding}$ is the binding energy of the electron, E_{photon} is the energy of the X-ray photons being used, $E_{kinetic}$ is the kinetic energy of the electron as measured by the instrument and $\emptyset$ is the work function dependent on both the spectrometer and the material. Each element can produce a characteristic set of XPS peaks at characteristic binding energy. These characteristic spectral peaks correspond to the electron configuration of the electrons within the atoms. The number of detected electrons in the characteristic peaks is directly related to the amount of element within the XPS sampling volume.

3.2.4 *Atomic force microscopy (AFM)*

The surface profile of the GQDs can be revealed by using atomic force microscopy (AFM) (Nanoscope IV AFM). The working principle of AFM is based on the intermolecular force between the tip and the specimen surface. The AFM consists of a sharp tip at the end of a flexible cantilever, which places several nanometers above the sample surface. The coordinate of the tip is determined by a laser source connected by a photodiode. When the tip is scanning along the surface, the cantilever deflects due to the roughness. The tip-surface interaction is monitored by reflecting laser beam off the back of cantilever into the photodiode detector. The photodiode records the change of the spot position and hence results in difference of output voltage, following by the determination of the oscillation amplitude. There is a feedback circuit to maintain a constant separation between the tip and surface in order to avoid the damage of both the tip as well as the sample.

3.2.5 *Fourier Transform infrared spectroscopy (FT-IR)*

Fourier Transform Infrared (FT-IR) Spectroscopy is able to investigate the structure of the GQDs. With the absorption characteristic and the natural vibration frequency within the range of IR, FT-IR is one of the significant techniques for structural analysis.

The FT-IR analysis was studied by MAGNA-IR 760 spectrometer with a revolution of 4 cm^{-1}. Infrared (IR) beam is transmitted through Michelson interferometer and then the sample, ultimately detected by IR detector. When the frequency of the IR reaches to the natural vibration frequency of the molecules in the sample, the IR will be absorbed by the corresponding molecules.

Interferogram is obtained as a result of intensity of IR against optical path difference. Consequently, the interferogram is Fourier transformed into IR spectrum with transmittance against wave number in cm^{-1}.

3.2.6 *UV-Vis absorbance*

The absorbance of the GQDs was measured by using a Shimadzu UV-2550 UV-vis spectrometer at room temperature. A light is excelled through a solution and recording how much light and what wavelengths were transmitted onto a photodetector. The wavelengths that were absorbed can be determined accordingly. The measurement of the solution and solvent (reference) are taken at same instant. The absorbance at given wavelength is calculated by

$$A = \log_{10} \frac{I_0}{I} \qquad \text{(Eq. 3.2)}$$

where I_0 is the transmitted intensity of light source, I is the intensity that makes it through the solution sample.

3.2.7 *Photoluminescence (PL)*

Photoluminescence (PL) is a technique in which a semiconducting material is excited to higher energy state by absorbing photons, and then it relaxes to a lower energy state and re-radiates photons. The radiation of the specimen depends on the band gap energy. The PL spectrum can be obtained by plotting the intensity of the emitted light from a sample excited by an appropriate excitation light source of same energy against wavelength.

The PL measurement mentioned in chapter 5 were measured by a Q-switched 355 nm Nd:YAG laser at pulsed operation (~ 6 ns, 10 Hz). The excitation

wavelength was adjusted from 300 to 430 nm using an optical parameter oscillator with beta barium borate (BBO). In chapter 6, the PL measurement was carried out by PL spectrometer (Edinburgh Instruments FLSP920). A continuous xenon arc lamp with spectral range of 230-2600 nm (ozone free) was used as the excitation source. The fluorescence signal recorded by the emission detector while the radiation was passing via the excitation monochromator. An appropriate filter is inserted between the sample and the photomultiplier, depending on which excitation wavelength was used. The light emitted from the sample is investigated by a monochromator. The absolute quantum yield measurement was carried out using integrating sphere (Edwinburgh Instruments, 150 nm in diameter coated with barium sulphate). During the quantum yield measurement, the sample was placed into the cuvettes inside the integrating sphere.

3.2.8 *Time-resolved spectroscopy*

PL decay kinetics profile was plotted as the luminescent intensity of the sample after excitation by a flash of light verses time [74]. The probability of radiative and non-radiative transitions from the excited state to the non-excited state can be studied. The time-resolved PL was measured by using a laser diode (pulse width: 48 ps) with excitation wavelength of 375 nm. The lifetime of the luminescence can be calculated according to luminescent decay curve. The decay curve can be fitted by a triple-exponential function

$$R(t) = \sum_{i=1}^{3} A_i e^{\frac{-t}{\tau_i}}, \qquad \text{(Eq. 3.2)}$$

where A_i is constant.

The average lifetime $<\tau>$ can be calculated according to

$$<\tau>=\frac{A_1\tau_1^2+A_2\tau_2^2+A_3\tau_3^2}{A_1\tau_1+A_2\tau_2+A_3\tau_3}. \qquad \text{(Eq. 3.3)}$$

3.2.9 *Two-photon luminescence*

Two-photon fluorescence is the process from which simultaneous absorption of two photons of identical or different frequencies in order to excite a molecule from ground state to a higher energy state. The energy difference between the lower and upper states of the molecule is equal to the sum of the energies of the two photons. It differs from linear absorption in that the atomic transition rate due to two photon absorption depends on the square of the light intensity, thus it is a nonlinear optical process. The two-photon fluorescence in our work was measured by femto second (fs) pulse tunable Ti:sapphire laser (Coherent, Chameleon). The wavelength and power of the laser can be tuned during the measurement.

3.2.10 *Single particle luminescence*

During the measurement, laser light (561 nm, 640 nm or 488 nm) was directed into a 1.49 NA Olympus ApoN oil-immersion (Type F, ne 1.518) 60X objective (Olympus America, Center Valley, PA, USA) mounted on an Olympus IX 81-inverted microscope (Olympus America). The intensity of the 561 nm laser was adjusted to ~78 W cm^2. Fluorescence emission was collected through the microscope objective and separated from the incident laser by using Green Filter set: laser cleaner: FF01-561-14, dichroic: Dio1-R488/561-25×36 emission: FF01-609/54-25 (Semrock, Rochester, NY, USA) or Red Filter set: Laser line cleaner: FF01-640-14, dichroic: Di02-R635-25x36, emission: BLP01-664R-25 or

Blue filter set: 51022 - EGFP/mRFP-1 from Chroma Inc. Data were typically collected for ~3-7 min at 100 ms exposure time by using a cooled (-80^{o}C) ANDOR iXon3 CCD camera (Andor Technology, South Windsor, CT USA) and Metamorph (Molecular Devices, LLC., Sunnyvale, CA, USA) software. All data were recorded at room temperature (25^{o}C). The shapes of the fluorescence spots are irregular because of fluorescence intensity fluctuations of the individual molecules and the number of molecules differs from frame to frame because of dark states. To overcome this we recorded 5 frames and then averaged the intensities and subtracted the background. Single-molecule events from wide field images were extracted from the stream acquisition of 2000 frames at 100 ms exposure time. This was done by integrating the intensity of 3×3 pixel area around isolated fluorescent spots using Metamorph or ImageJ (NIH, USA) and then subtracting the background.

Chapter 4 Characterizations of GQDs

4.1 *GQDs synthesized by domestic microwave oven*

4.1.1 *Structural properties*

Fig. 4.1 (a) shows the size distribution of the GQDs. The average diameter of the GQDs is 3.4 nm and the size distribution accords well with Gaussian distribution. The full-width-at-half-maximum (FWHM) of the fitted Gaussian curve is 0.55 nm, indicating the narrow distribution nature of the GQDs. Figure 4.1 (b) shows the AFM image of the monodispersed GQDs, four GQDs are selected randomly and labeled as 1, 2, 3, and 4. The average height of these GQDs is 3.2 nm as shown in Figure 4.1 (c).

Fig. 4.1 (d-g) shows the TEM images of the GQDs. The images reveal spherical shaped and monodispersed GQDs. The HRTEM images as shown in Figure 4.1 (f) and (g) indicate that the lattice spacing of the GQDs is about 0.33 nm, corresponding to the (002) facet of graphite [16]. The sizes of the GQDs prepared at 1 and 5 min microwave irradiation times are about 1.8 nm and 4.8 nm respectively as shown in Figure 4.1 (f) and (g). The size of the GQDs is influenced by the microwave irradiation time. The average diameter of the GQDs can be tuned from 1.8 to 21 nm when the irradiation time is increased from 1 to 9 minutes (Figure 4.1(h)) respectively.

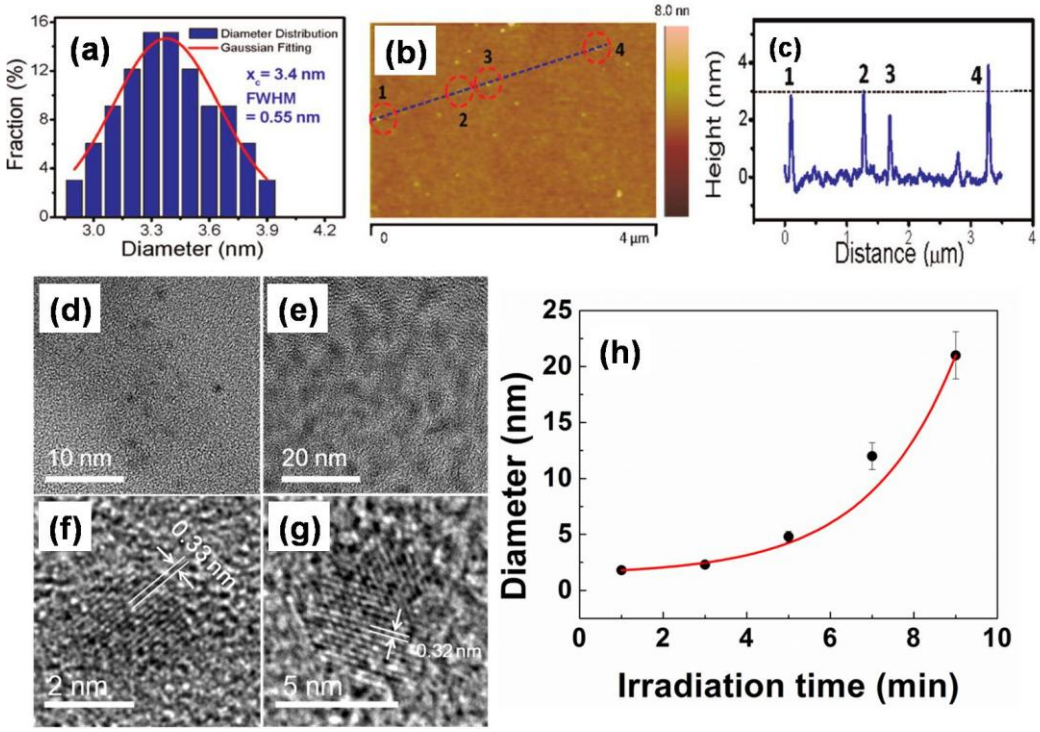

Figure 4.1 (a) The diameter distribution of the GQDs, the red line is the Gaussian fitting curve. (b) AFM image of the GQDs. (c) The height distribution of the GQDs as shown in AFM image. TEM images of the GQDs prepared at (d) 1 and (e) 5 minutes. (f and g) HRTEM images of the GQDs prepared at 1 and 5 minutes respectively. (h) Size distribution of the GQDs at various microwave irradiation time.

FTIR spectroscopy was used to investigate the bonding composition of the GQDs and its functional groups. Figure 4.2 (a) shows the FTIR spectra of the GQDs prepared by various source concentrations and microwave heating times. An obvious absorption peak centered at 1641 cm^{-1}, which is caused by C=C stretching, is observed. Under the reaction process, glucose is dehydrated to form C=C which is the elementary unit of the GQDs. A sharp absorption peak at 852 cm^{-1} from the source glucose is due to CH_2 rocking. Such a peak becomes much weaker from the GQDs spectrum, indicating a drastic decrease in H after the

formation of GQDs. The broad peak centered at 3392 cm^{-1} reveals O-H bonding. The absorptions at 1027 and 1076 cm^{-1} are attributed to ν_{C-O}; absorptions at 1360 and 2927 cm^{-1} also reveals the existence of C-H.

We carried out XPS characterization to further confirm the functional groups on the surface of the as-prepared GQDs. Figure 4.2 (b) shows the XPS spectrum of C1s. The measured spectrum can be deconvoluted into five surface components, corresponding to sp^2 (C=C) at binding energy of 284.5 eV, sp^3 (C-C, and C-H) at 285.5 eV, C-OH at 286.6 eV, C-O-C at 287.2 eV, as well as C=O at 288.6 eV. It should be noted that the XPS data presented here represent the surface components of the GQDs, thus the relative contents of the core component (C=C) of the GQDs cannot be obtained. The surface components of the GQDs as determined by the XPS are in good agreement with FTIR results.

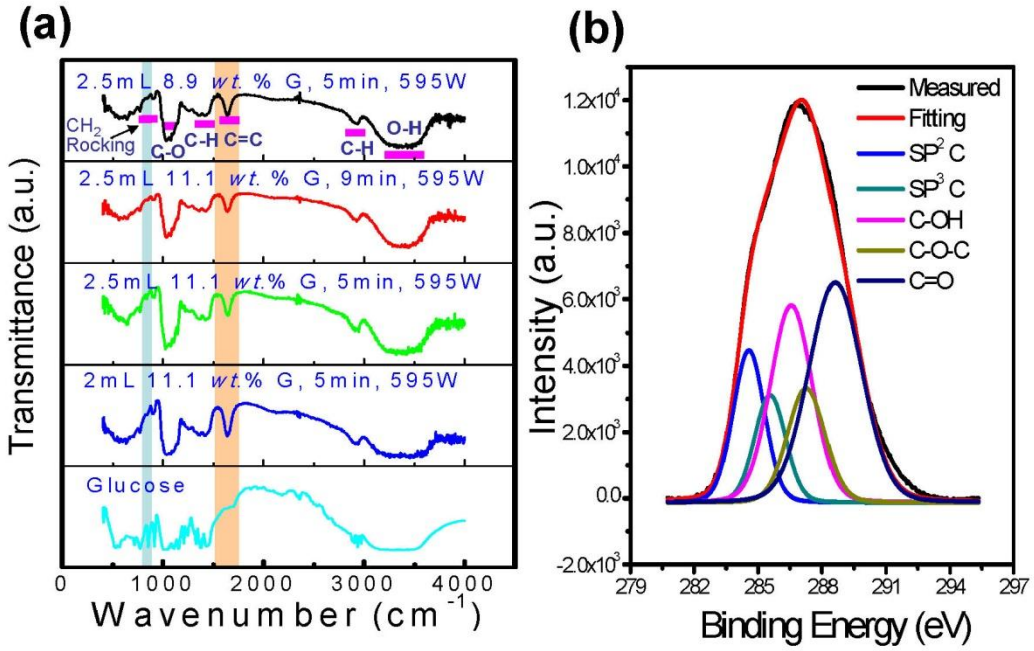

Figure 4.2 (a) FTIR spectra of the source glucose and the GQDs prepared under different conditions. All the GQDs prepared under different conditions show similar IR absorption peaks. (b) The C1s XPS spectrum of the GQDs. The GQDs were prepared with 11.1 wt % glucose solution for 9 min at 595 W microwave heating.

4.1.2 *Optical properties*

The absorbance of the GQDs prepared under various reaction times is shown in Figure 4.3 (a). All the GQDs show two obvious absorption peaks centered at 228 and 282 nm. Surprisingly, the two absorption peaks are independent of the size of the GQDs. Figure 4.3 (b) shows the photoluminescence (PL) spectra of the GQD solution. A broad emission peak at 473 nm is observed when the sample is excited by 375 nm. The PL peak shifts from 473 to 519 nm when the excitation wavelength changed from 375 to 450 nm. However, the PL intensity decreases as

the PL peak red-shifted. It is worth noting that the size-independent PL of the GQDs is observed as shown in Figure 4.3 (c). In agreement with the absorbance results (Figure 4.3 (d)), the peak position of the emission PL does not change with the size of the GQDs. The size-independent PL of the GQDs could be related to the self-passivated layer of the GQDs. Figure 4.3 (d) shows a series of GQD solutions irradiated by the ambient (top) and UV lamp (bottom). The solutions were prepared by various heating times. Although the size of the GQDs increases with heating time, the emission color of the solutions does not change obviously.

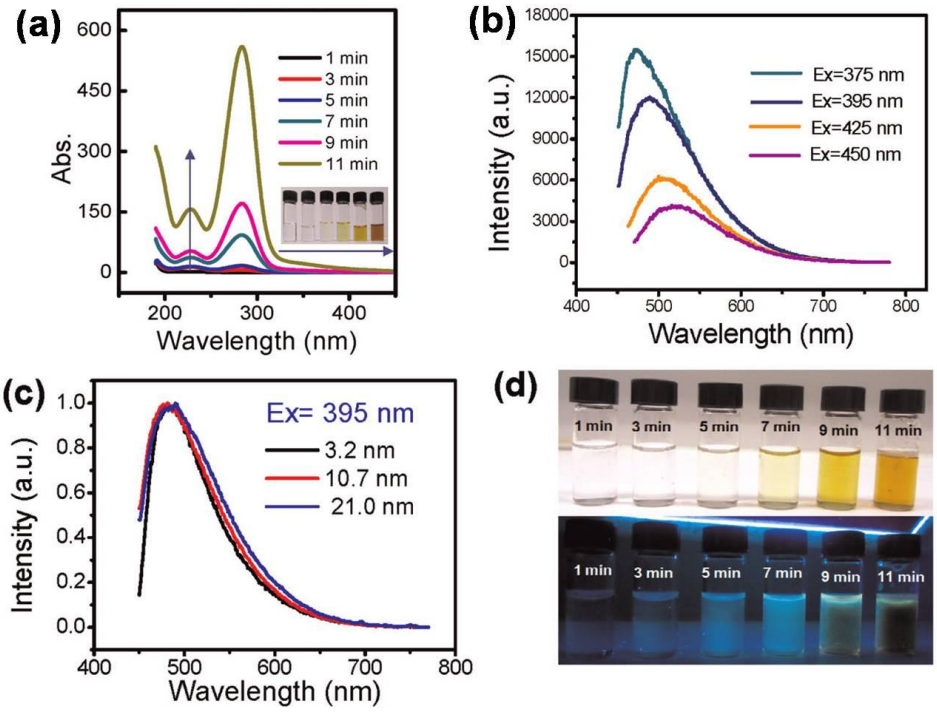

Figure 4.3 (a) The effect of microwave heating time on the absorbance of the GQDs. (b) The PL spectra of the GQDs excited by various wavelengths. (c) the normalized PL spectra of the GQDs with various sizes. (d) the GQDs solutions irradiated by ambient light (top) and 365 nm UV lamp (bottom).

The self-passivated layer on the surface of the GQDs should play an important role in the observed emission. As demonstrated above, our GQDs consist of C=C core, as well as O and H containing functional groups on the surface. The functional groups (C-OH, C=O, C-O-C, C-H) on the surface of the GQDs form "surface states" which are the energy levels between π and π* states of C=C. Because of the difference in chemical bonding between C=C and C=O groups, the variation of π* energy states is expected. Thus a distribution π* band (C=C and C=O) is resulted. Different kinds of functional groups (C-OH, C=O, C-O-C, C-H) are presented on the surface of the GQD, forming "surface states" energy levels between π and π* states of C=C. The functional groups have various energy levels, which may result in a series of emissive traps. When a certain excitation wavelength illuminates the GQDs, a surface state emissive trap will dominate the emission. As the excitation wavelength changes, another corresponding surface state emissive trap will become dominant.

4.2 *GQDs synthesized by microwave reactor*

4.2.1 *Structural properties*

Figure 4.4 shows the typical TEM images of the GQDs dispersed on the copper grid. The images revealed highly monodispersed property of the GQDs, which is one of the major advantages of our GQDs preparation method [16]. The presence of lattice fringe of 0.247 nm, which corresponds to the basal plane distance of bulk graphite [16], is shown in the inset of Figure 4.4 (a). The average size of the GQDs is 3.42 ± 0.15 nm when the reaction pressure is 165 psi. As the reaction pressure increased to 350 psi, the size of the GQDs increased from 3.4 to 11.9 nm. The surface morphology of the GQDs dispersed on the SiO_2/Si substrate was

studied by atomic force microscopy (AFM). Figure 4.4(c) shows three randomly selected GQDs labeled as A, B and C. The average height of these GQDs is about 3.2 nm, corresponding to a few atomic layers (~ 5 layers) GQDs.

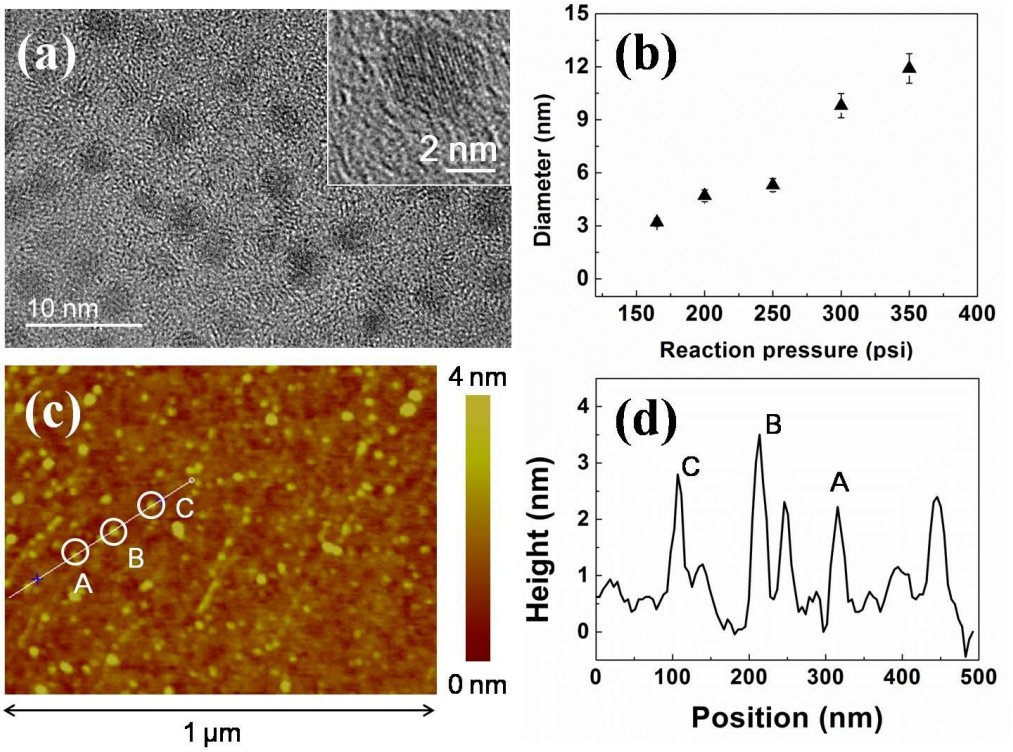

Figure 4.4 (a) High-resolution TEM image of the GQDs. (b) The diameter of the GQDs for various reaction pressures. (c) AFM image of the GQDs. (d) The height analyses of the GQDs as shown in AFM image (c).

The functional groups of the GQDs were identified using FT-IR spectroscopy, as shown in Figure 4.5 (a). The spectrum of the GQDs exhibits a C=C stretching at 1641 cm^{-1}, which is an elementary unit of the GQD core. An O-H stretching can be observed at the peak of 3392 cm^{-1}. The existence of C-O in the GQD is confirmed by the presence of absorption bands at 1026 and 1076 cm^{-1}. The absorption bands at 1415 and 2929 cm^{-1} are resulted from the C-H bonding. We performed XPS on the samples to determine the surface composition of the

GQDs, as shown in Figure 4.5 (b). The measured C1s spectrum can be fitted with five components, such as 284.5 eV (sp^2 bonded carbon), 285.3 eV (sp^3 bonded carbon), 286.5 eV (C-OH group), 287.1 eV (C-O-C group) and 288.1 eV (C=O group).

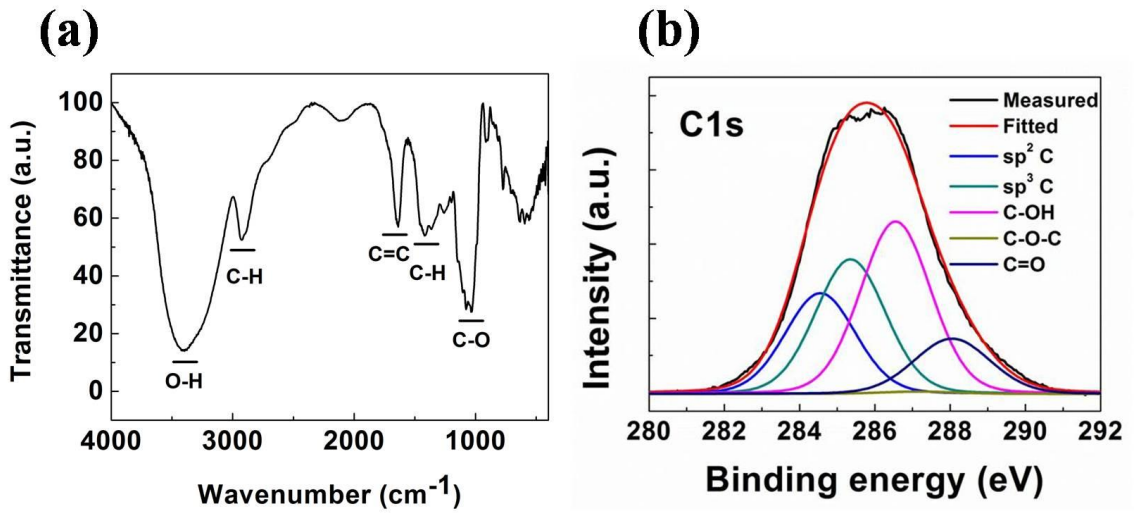

Figure 4.5 (a) FT-IR spectrum and (b) C1s XPS spectrum of the GQDs.

The growth mechanism is similar to that of using domestic microwave oven. Herein, the GQD size is dependent on the reaction pressure. At first glance, glucose molecules undergo carbonizing, nucleating, crystallizing and growing up. Since the core of the GQD is composed of C=C bonding, the functional groups can only exist at the surface of the GQD, as confirmed by FT-IR and XPS spectra. Hence the growth occurs only at the interface of the GQD. Because of the high pressure induced by the hydrothermal condition, the C=C bonding is arranged in an orderly manner and assist in the growth of crystalline GQD. As the pressure increases, the growth rate of the GQD becomes faster. The existence of the hydrophilic functional groups such as –OH, C-O-R and –C=O on the surface makes the GQDs water soluble.

4.2.2 *Optical properties*

Fig. 4.6 shows the PL behaviors of the GQDs. As shown in Fig. 4.5 (a), the PL shifts from 440 nm to 554 nm when the excitation wavelength changed from 330 nm to 470 nm, which has similar trend with the GQDs prepared by domestic oven. The emission of the GQDs can be tuned by changing the size of the GQDs (Figure 4.5 (b)). This observation is different from those by domestic microwave oven. It is clearly seen that the PL emission is shifted from 456 to 598 nm with increasing GQD size, which demonstrated similar trend observed in other quantum dots due to quantum confinement effect [60]. It is suggested that the observed different emission from the different-sized GQDs is the result of variation in the nature of sp^2 bonding and density available at the GQDs [75].

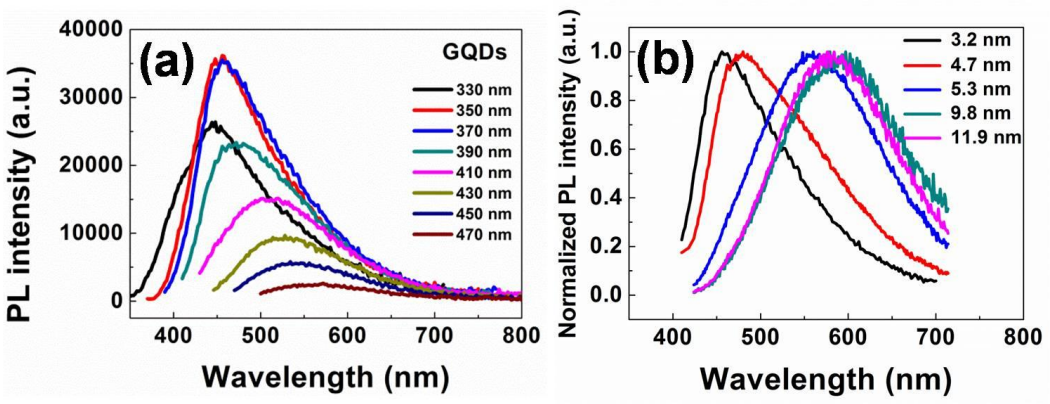

Figure 4.6 (a) The excitation dependent PL emission of GQDs. (b) Size dependent PL of GQDs. The GQDs were excited by 365 nm.

Chapter 5 GQD-agar Composite

5.1 *Introduction*

In previous chapter, it has been demonstrated that the GQDs exhibited excellent luminescence properties. Hence, it is necessary to stabilize the GQD solution by converting them into a thin film in order to utilize the highly fluorescent GQDs. The typical approach is the incorporation of quantum dots (QDs) into certain polymer films such as styrene and methylmethacrylate [76]. However, stabilizing QDs into the bulk polymer remains a challenge, especially for the QDs stored in aqueous solution. Phase separation and aggregation of QDs would occur and this would lead to luminescence quenching. Meanwhile, QD/polymer composites have been fabricated by pre-polymerization of monomer QD solution to avoid the separation of QDs from the polymer matrix [77]. The main disadvantage of this method is complicated process and time-consuming for the polymerization (> 15 hours). Recently, it has shown that QD/polymer can be formed based on covalent attachment mechanism by adding small amount of solvent. However, the luminescence of the QDs is quenched and only few QDs survive [78]. Herein, we demonstrate a facile route to fabricate fluorescent GQD/polymer composites by using polysaccharides such as agar, which is widely used as gel-forming agents, water-holding agents and stabilizers in food industry. We fabricated GQD-agar composites by directly dispersing agar flakes into the GQD solutions. No fluorescent quenching on the GQD-agar composite is observed. Moreover, a white light-emitting diode (WLED) was demonstrated by coating GQD/agar composite onto a blue emitting LED. The WLED exhibited over ~58% light-conversion efficiency and over 100-hour colour stability.

5.2 *Experimental*

Preparation of GQD-agar composite: 10 mg of agar flakes (Chancevon Agar) was inserted into 2 mL of the GQD solution at 85°C under vortex mixing. The mixture was well stirred and heated until it became homogeneous with the solution. Subsequently the mixture was poured into a 0.8 cm diameter glass tube mound and was cooled down to room temperature under ambient atmosphere.

Characterization method: The electroluminescence of the GQD-agar LED was measured by Ocean Optics USB4000 fiber optic spectrometer at room temperature. An integrated sphere was used in the assessment of luminous efficiency, colour rendering index and correlated colour temperature. To determine the light conversion efficiency of the white LED, the wavelength was firstly converted to photon energy, and followed by the integration of the emission spectra to obtain the peak areas of blue and GQD emission. As a result, the conversion efficiency can be calculated by the ratio of the GQD emission area to total area of the blue and GQD emission.

5.3 *Results and discussion*

5.3.1 *Structural properties*

FTIR spectra of the GQD solutions and composites are shown in Fig. 5.1 (a). The FTIR spectra of the GQDs remain unchanged for the GQDs prepared at the irradiation time of 3 to 7 minutes. The FTIR spectrum of the GQD-agar composite is dominated by the agar. Nevertheless, no chemical bonding between the GQDs and the agar molecules is found. XPS was carried out to further confirm the functional groups on the GQD-agar composite surface. The XPS spectra of the GQD-agar composite and pure agar are shown in Fig. 5.1 (b). The

shape and intensity of the C1s peak for the composite and agar are almost identical, further confirming that no chemical bonding was formed between the GQDs and agar molecules.

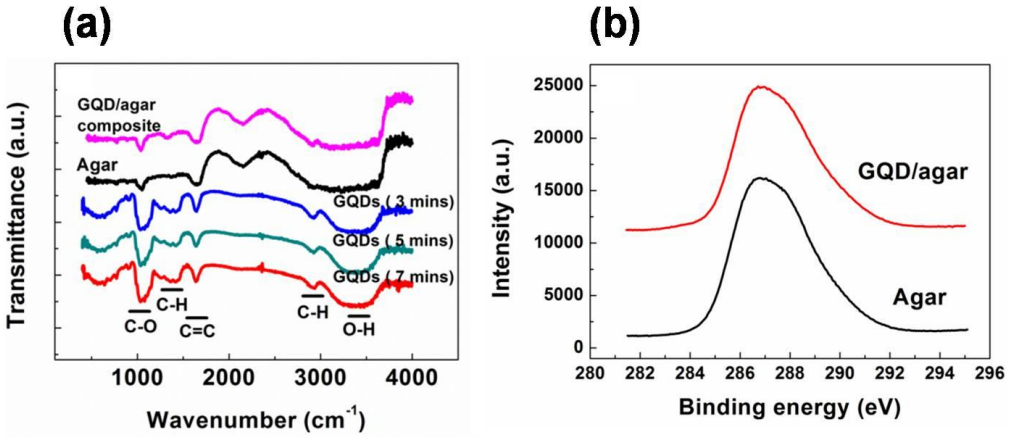

Figure 5.1 (a) FTIR spectra of the GQD solutions, GQD–agar composite and agar. C1s XPS spectrum of (b) the GQD–agar composite and agar. The GQD solutions were prepared by 5 min microwave irradiation.

5.3.2 *Optical properties*

Fig. 5.2 (a) shows the ultraviolet-visible (UV-vis) absorption spectra of the GQD–agar composites. Since saturated absorption in the UV range was observed in the GQD solutions [11], the composites were prepared with the GQD solutions diluted with 6.4-fold. The intensity of the absorbance of the composites is found to increase with the irradiation time. In addition, strong absorption is observed over the wavelength from 200 to 300 nm. The absorption band peak at 228 nm is related to the $\pi \rightarrow \pi^*$ transition of the aromatic C=C bond, while the absorption band at 282 nm represents the $n \rightarrow \pi^*$ transition of the C=O bond [79]. Compared with the absorption spectrum of agar, the peaks of 228 nm and 282 nm in the composites are attributed to the GQDs. The PL spectra of the GQD-

agar composites prepared at various irradiation times are shown in Figure 5.2 (b). All samples exhibit a blue emission band peaked at 474 nm when an excitation wavelength of 375 nm is used. The full width at half maximum (FWHM) of the PL spectra is ranging from 90 to 109 nm. There is no PL shift after the incorporation of agar into the GQDs by comparing the spectrum with the parent GQD solutions [11]. In order to further investigate the optical properties of the GQD-agar composites, a detailed PL measurement was carried out with different excitation wavelengths, as shown in Figure 5.2 (c). The PL peak at 433 nm was observed when the excitation wavelength of 300 nm is used. The peak is shifted to 530 nm when the excitation wavelength is adjusted to 430 nm. The excitation-dependent emission wavelength is a common phenomenon reported in carbon-based QDs [80-83]. In our works, the excitation-dependent emission of the GQDs has been explained in terms of surface states formed by functional groups located at the surface of the GQDs, resulting in various emission traps. Different surface-state emissive traps are emerged with various excitation wavelengths [11].

In order to study the optical properties of the samples at a function of dilution fold, the GQD solutions were diluted with different folds of deionized water. For each dilution fold, the GQD-agar composite was fabricated with the same amount of agar. Figure 5.2 (d) shows the PL lifetime and quantum yield (QY) of various dilution folds ranging from 0 (no dilution) to 11 folds. The PL lifetimes of the GQDs and composites increase with the increase of dilution fold. The lifetimes of the GQDs (2.9 – 3.8 ns) are shorter than the GQD-agar composites (3.5 – 4.5 ns). In addition, the GQD solutions and composites with a high dilution fold show higher QY, presumably owing to the self-quenching resulted

from reabsorption of the high concentration GQDs [84]. From the result shown, the largest QY for the GQD solution and composite can be as high as 12% at ~ 9 fold dilutions, indicating that there is no PL quenching in the agar embedding process.

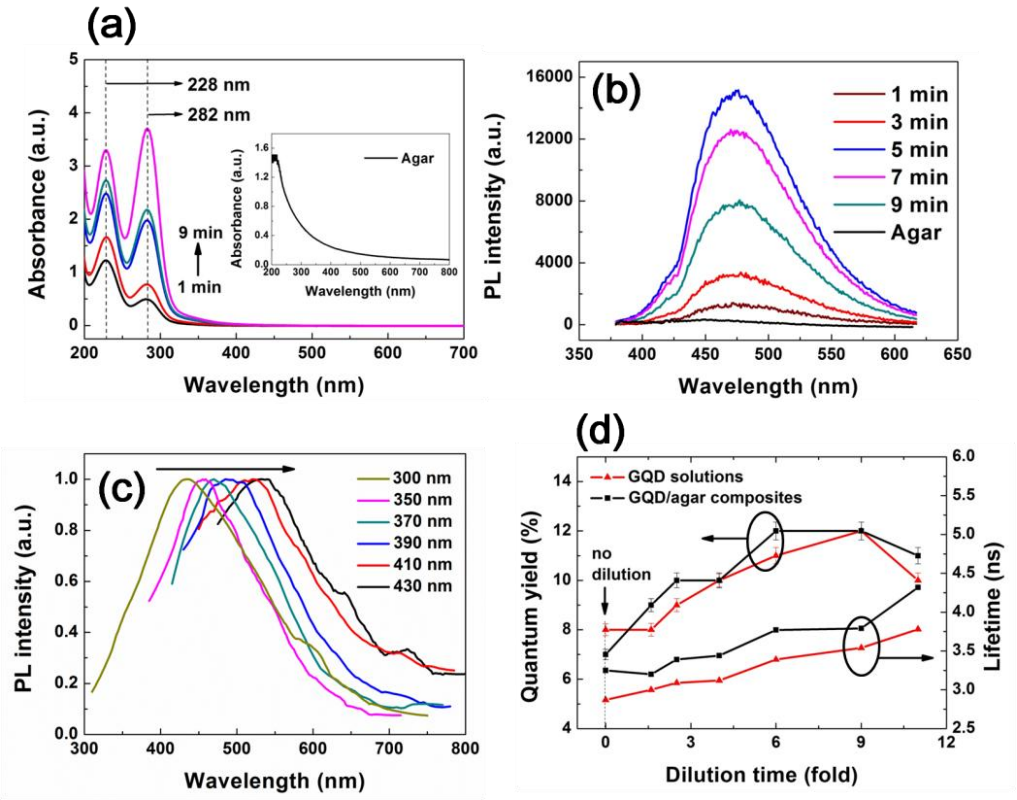

Figure 5.2 (a) UV-vis spectra of the GQD-agar composites. The inset shows the absorbance spectrum of the agar. (b) PL spectra of the GQD-agar composites prepared at various microwave irradiation times. The excitation wavelength is 375 nm. (c) Excitation-dependent normalized PL of the GQD-agar composite. (d) Plot of quantum yield and lifetime of the composite as a function of dilution fold.

Time-resolved PL decay of the GQD-agar composite is shown in Fig. 5.3. The lifetime contains a fast component (~ 0.8 ns) and two slow components (~ 3.0 ns and ~ 14 ns). The average lifetimes of the GQD-agar composite ranging from 3.5

ns to 4.4 ns for various emissions are tabulated in Table 5.1. The results are consistent with the reported values (4 - 9 ns) of the carbon dots prepared by laser ablation [85] and pyrolysis method [86].

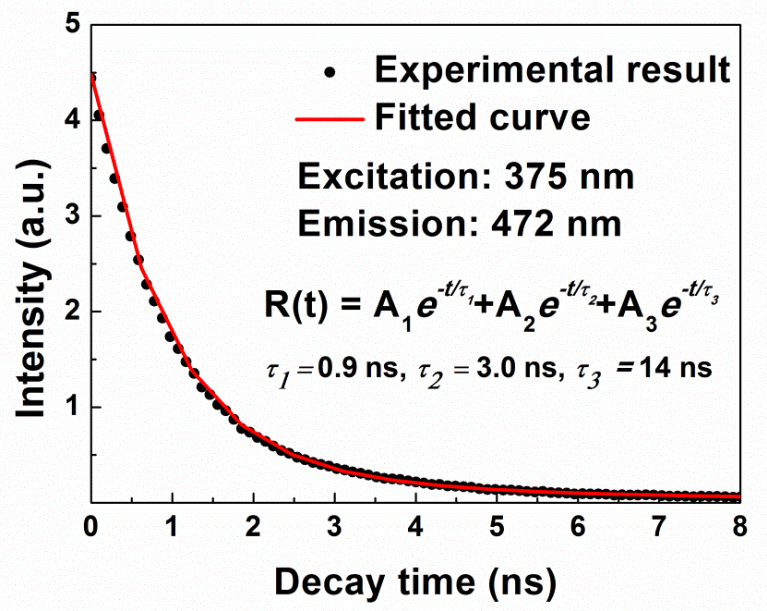

Figure 5.3 Time-resolved PL spectra of the GQD-agar composite. The GQDs were prepared under microwave irradiation time of 5 minutes.

Emission	τ_1(ns)	τ_2(ns)	τ_3(ns)	$<\tau>$(ns)
440 nm	0.83	2.30	15.86	3.52
444 nm	0.88	2.56	19.38	3.25
472 nm	0.89	2.90	14.15	3.47
507 nm	1.02	3.56	13.39	3.99
513 nm	1.02	3.39	11.82	3.96
527 nm	0.98	3.42	12.21	4.35

Table 5.1 Summary of the average lifetimes of the GQD-agar.

5.3.3 *White LED characteristics*

Figures 5.4 (a) and (b) show the fluorescent photos of the GQD solutions and GQD-agar composites prepared at various microwave irradiation times. The surprisingly strong PL emissions of these composites make it a novel fluorescent material for optoelectronic applications. Thus, the as-prepared GQD-agar composites were utilized as a light conversion material in a commercial blue LED with peak emission of 410 nm, as shown in Figure 5.4 (c) and (d). The corresponding electroluminescent (EL) spectra of the composite-coated LED under various forward currents are shown in Figure 5.4 (e). The emission peaks of the blue LED chip and the GQD-agar composite were located at 410 nm and 524 nm respectively. The GQD emission intensity of the underlying blue LED can be tuned by adjusting the amount of the GQDs incorporated in the agar. Both the blue and green emission intensities increase steadily with the applied voltage which reveals the LED with stable light conversion and colour quality. In order to verify that the emission peak at 524 nm is due to the excitation wavelength of the LED (i.e. 410 nm), the corresponding composite was excited by a 410 nm. The PL spectrum of the composite is shown in Figure 5.4 (f) for comparison with the EL spectrum of the composite coated-LED. It is shown that the PL peak of the composite is matched very well with the 524 nm peak from the EL spectrum. In addition, no emission peak located at 524 nm is observed in both EL spectra of the pristine LED and agar-coated LED (Figure 5(g)). Thus the 524 nm peak is originated from the composite.

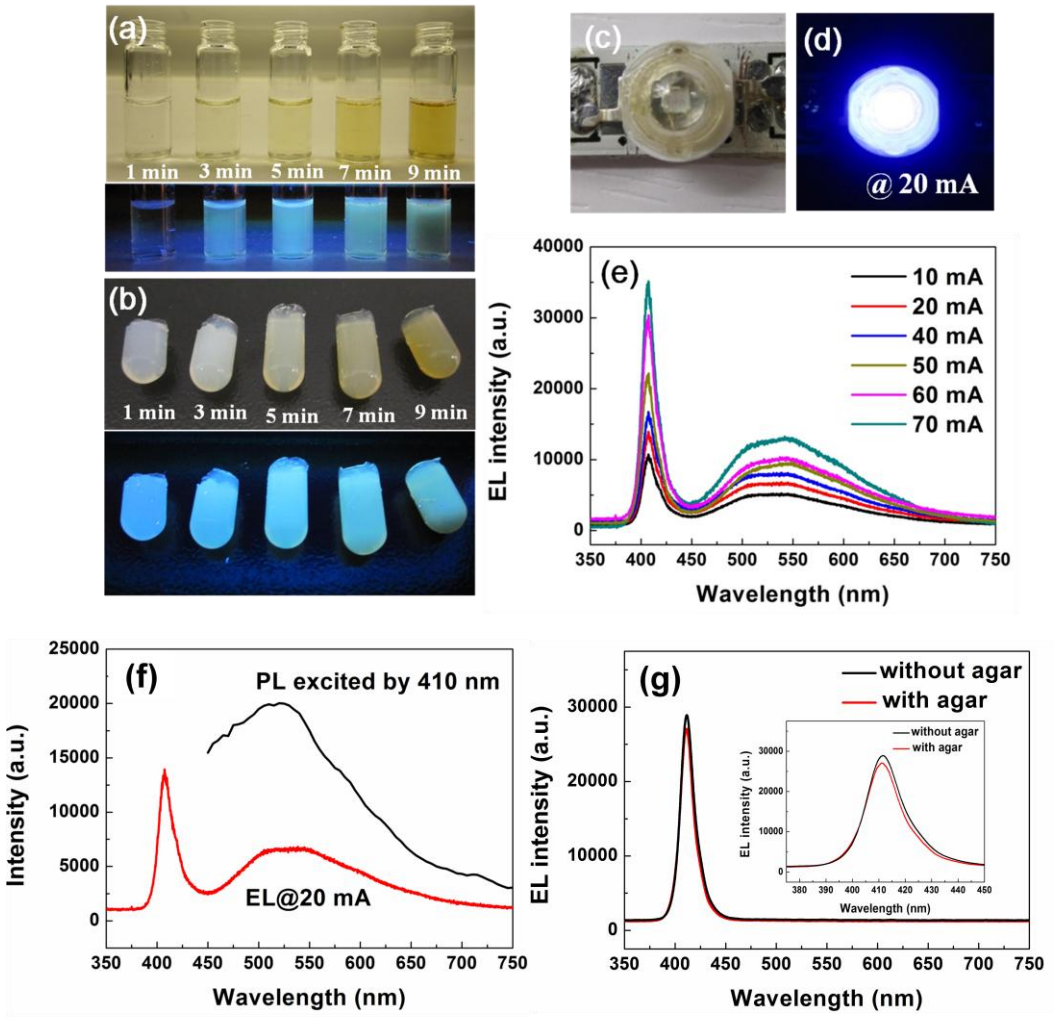

Figure 5.4 Fluorescence images of (a) the GQD solutions and (b) GQD-agar composites. The photograph of the as-fabricated WLED (c) without and (d) with biased current. (e) EL spectra of the WLED under various forward currents. (f) PL spectrum of the GQD-agar composite; EL spectrum of the WLED operated at 20 mA. (g) EL spectra of the blue LED and that coated with agar.

The luminous efficiency and light-conversion efficiency of the GQD-agar composite-coated LED at different forward currents are shown in Figure 5.5 (a). The luminous efficiency of the composite-coated LED is 42.2 lm W^{-1} under 20 mA forward current, while that of the blue LED is 12.7 lm W^{-1}. Although a slight decrease from 43.2 to 38.8 lm W^{-1} in luminous efficiency is observed when the

forward current increases from 10 mA to 70 mA, the luminous efficiency of the composite-coated LED is higher than that of the reported QD-based LEDs [87, 88]. The colour rendering index (CRI) and correlated colour temperature (CCT) of the composite coated LED were determined to be 72.0 and 5532 K, corresponding to cool white colour. The light conversion (blue-to-GQD emission) efficiency of the WLED is 61.1 % under 20 mA of forward current and remains nearly constant with increasing current. The result reveals that the GQD-agar composite exhibits superior light conversion stability as compared to the recent reported CIS/ZnS-QD based WLED [88]. The change of light conversion efficiency was monitored while the WLED was operated at 20 mA under ambient condition without any heat sink. The light conversion efficiency of the WLED is almost constant for over 100 hours of continuous operation as shown in Figure 5.5 (b). The CIE (International Commission on Illumination or Commission Internationale de I'Eclairage) coordinates of the LED was changed from (0.26, 0.20) to (0.33, 0.38), and no obvious change of CIE coordinates was observed at different applied currents, indicating good colour stability of the output light (Fig. 5.5 (c)). From the results shown, the GQD-agar composites exhibit excellent light converting properties and stability as compared to other semiconductor-based QDs and phosphors [89-93]. Our toxic-element-free GQDs with stable optical properties make it a promising alternative for a wide range of optoelectronic applications.

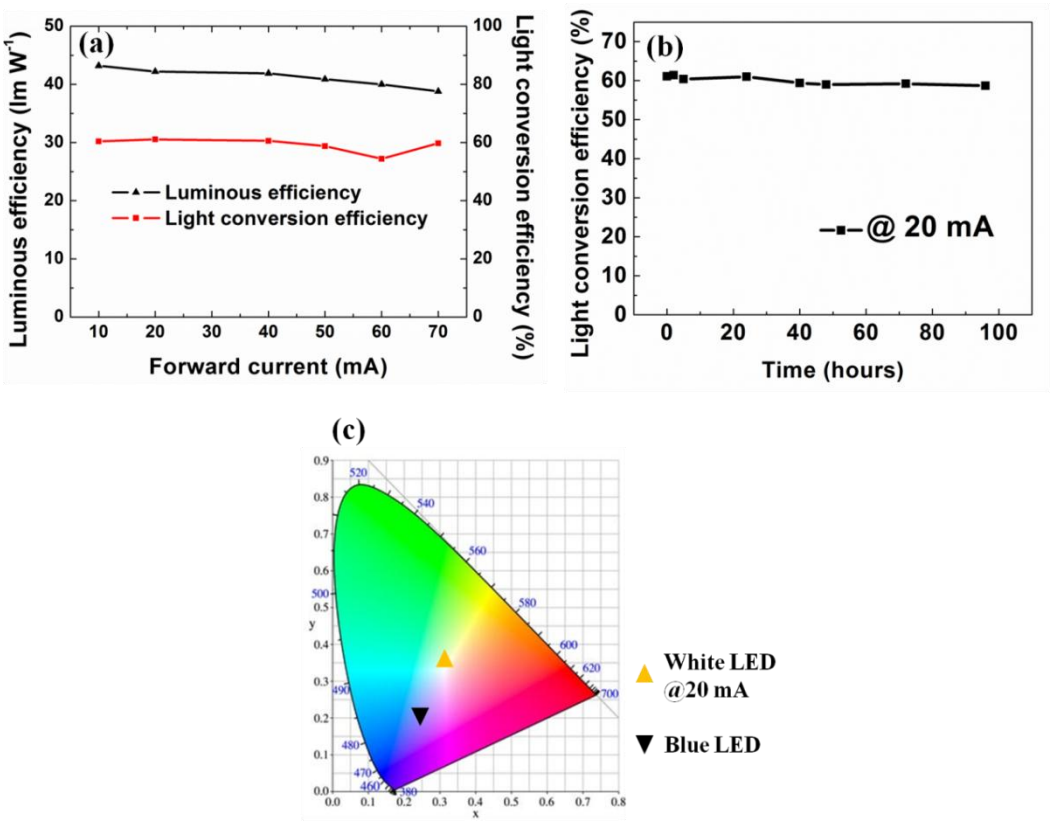

Figure 5.5 (a) The luminous efficiency and light conversion efficiency against forward currents. (b) The light conversion efficiency of the WLED operated at 20 mA as a function of time. (c) CIE coordinates of the blue and WLED operated at 20 mA.

5.4 *Summary*

In summary, we have demonstrated a facile method for preparing GQD/agar composite. There is no obvious change in optical properties when incorporating the GQDs into agar. A white GQD-agar-LED was fabricated by coating the GQDs/agar composite onto the blue LED. The WLED showed superior performance with a CIE 1931 coordinates of (0.33, 0.38), luminous efficiency of 42.2 lm W^{-1}, CRI of 72.0, CCT of 5532 K at 20 mA forward current. The light conversion efficiency of the white LED reached up to ~ 61 % and was

maintained for continuous operation under ambient conditions. The results demonstrated that the GQD-based WLEDs could be a promising solution for solid-state lighting.

Chapter 6 Electrical Hysteresis of PANI-GQD Composite

6.1 *Introduction*

Nanocomposite materials with the combination of nanoparticles and polymer have demonstrated superior electrical, optical and mechanical properties [94-101]. The general obstruction to the large-scale production and commercialization of nanocomposites is the lack of cost effective methods for controlling the dispersion of nanoparticles in the polymer matrix. It is because nanoparticles typically aggregate, in turn, it restricts the benefit of size-dependent properties of nanoparticles. The lack of structure-related properties of nanocomposites is another reason for the limited application [96]. Hence, it is of great interest to study various kinds of nanoparticle-polymer composite having different nanoparticles sizes and shapes. Among various conducting polymers, such as p-phenylenevinylene (PPV), polypyrrole (PPy) and polyaniline (PANI), PANI is an unique and promising polymer for practical applications due to its simple preparation, environmental stability, low cost and reversible control of electrical properties by both charge-transfer doping and protonation [102, 103]. Recent studies have demonstrated that incorporation of various nanomaterials into PANI matrix is able to alter the electrical properties and mechanical properties of the polymer matrix. For instance, Zhu *et al.* [104] prepared functional-multiwall carbon nanotubes MWCNT/PANI composite films which were synthesized by electrochemical co-deposition. Berzina *et al.* [105] synthesized gold nanoparticles/PANI composite materials by the polymerization

of anilinium, and this resulted in the formation of Schottky barriers between PANI and gold particles.

The bistable electrical conductivity of the composites with 1D nanostructures and organic materials has been reported [106-108]. The mechanisms of electrical bistability and memory effect are dependent on the material system [109-112]. It is worthwhile to investigate the electrical properties of composites that are based on 0D system. In this chapter, we have demonstrated a facile, low-cost synthesis in which the PANI-GQD composite can be prepared through a chemical oxidation polymerization process. The luminescence of the GQDs was found to be tunable by varying the content of the PANI. Furthermore, the electrical hysteresis behavior of the composite was observed. The hysteresis effect of the device can be tuned by the concentration and the size of the GQDs.

6.2 *Experimental*

Preparation of PANI-GQD composite: Hydrochloride acid (HCl; 37%) was dispersed in the aniline to form anilinium salt solution by protonation of aniline monomer. The GQD solution was directly added to the salt solution with different mole numbers of aniline. The mixture was heated at 80 ℃ for 30 minutes and then cooled to room temperature. The anilinium ions were attached to the GQDs in the aqueous solution under thermal annealing via charge-charge interactions. The ammonium persulfate (APS) was purified before adding to the mixture. The purification procedure is described as followed: (i) the massive amount of APS powder was dissolved in DI water to reach a saturated solution. (ii) The solution was cooled at 0 ℃ for more than 1 hour. (iii) Re-crystallization of APS was obtained. (iv) The APS crystals were filtered and dried at 50 ℃.

Subsequently, the polymerization was taken place at 4 ℃ for 30 minutes. The obtained dark green dispersion was centrifuged at 10000 rpm for 15 minutes. The synthesis process is shown in Figure 6.1 (a). For comparison, pure PANI was also synthesized under the same reaction condition.

Characterization: In order to study the electrical characteristics of the composite, 0.5 mL of the solution was drop-casted on the ITO glasses. The ITO glasses were completely covered by the solution. The films were kept at room temperature for 24 hours and then annealed at 75℃ for 2 hours. The patterned gold electrodes with a thickness of 100 nm were fabricated by thermal evaporated deposition. The current-voltage measurements were carried out using probes station with a programmable electrometer Keithley (model 2400).

6.3 *Results and discussion*

The functional groups of the PANI-GQD were identified using FT-IR spectroscopy, as shown in Figure 6.1 (b). The peaks at 1490 cm^{-1} and 1396 cm^{-1} are ascribed to the stretching vibration of benzenoid ring and C-N of the aromatic secondary amines. The peak at 1139 cm^{-1} is attributed to the in-plane bending vibrations of the benzene ring. Almost all the FT-IR peaks of the PANI are maintained. However, these peaks shifted to higher frequencies at 1502 cm^{-1} (benzenoid ring), 1402 cm^{-1} (C-N of the secondary amines) and 1199 cm^{-1} (in-plane benzene ring) respectively. This might be explained by the conjugation between the GQDs and PANI. In addition, the peak at 1052 cm^{-1} (the C-O characteristics peak of GQDs) appears in the spectrum of PANI-GQD, which suggests that the oxygenated functional groups on the GQDs play an important role in the formation of the composites.

Complementary to the FT-IR results, the UV-Vis absorption spectra of the GQDs and composites are shown in Figure 6.1 (c). Two strong UV absorption peaks at 228 and 284 nm are found in the GQD spectrum. The peak at 228 nm is caused by π to π^* transition of C=C, while the peak at 284 nm is attributed by n to π^* transition of the C=O bond [79]. The PANI-GQD composite shows mainly four characteristic peaks at 236, 284, 420 and 850 nm. The first two peaks (236 and 284 nm) were derived from the GQDs. The shift of the peak from 228 to 236 nm of GQDs might be attributed to the conjugation between the GQDs and PANI [114]. The other peaks at 420 and 850 nm were attributed to the polarization zone transition of PANI [115]. Furthermore, the ratio of the peak of C=O to that of C=C transition in the composite became smaller in comparison of the GQDs. The above results showed that the GQDs and PANI conjugate existed in the PANI-GQD composite.

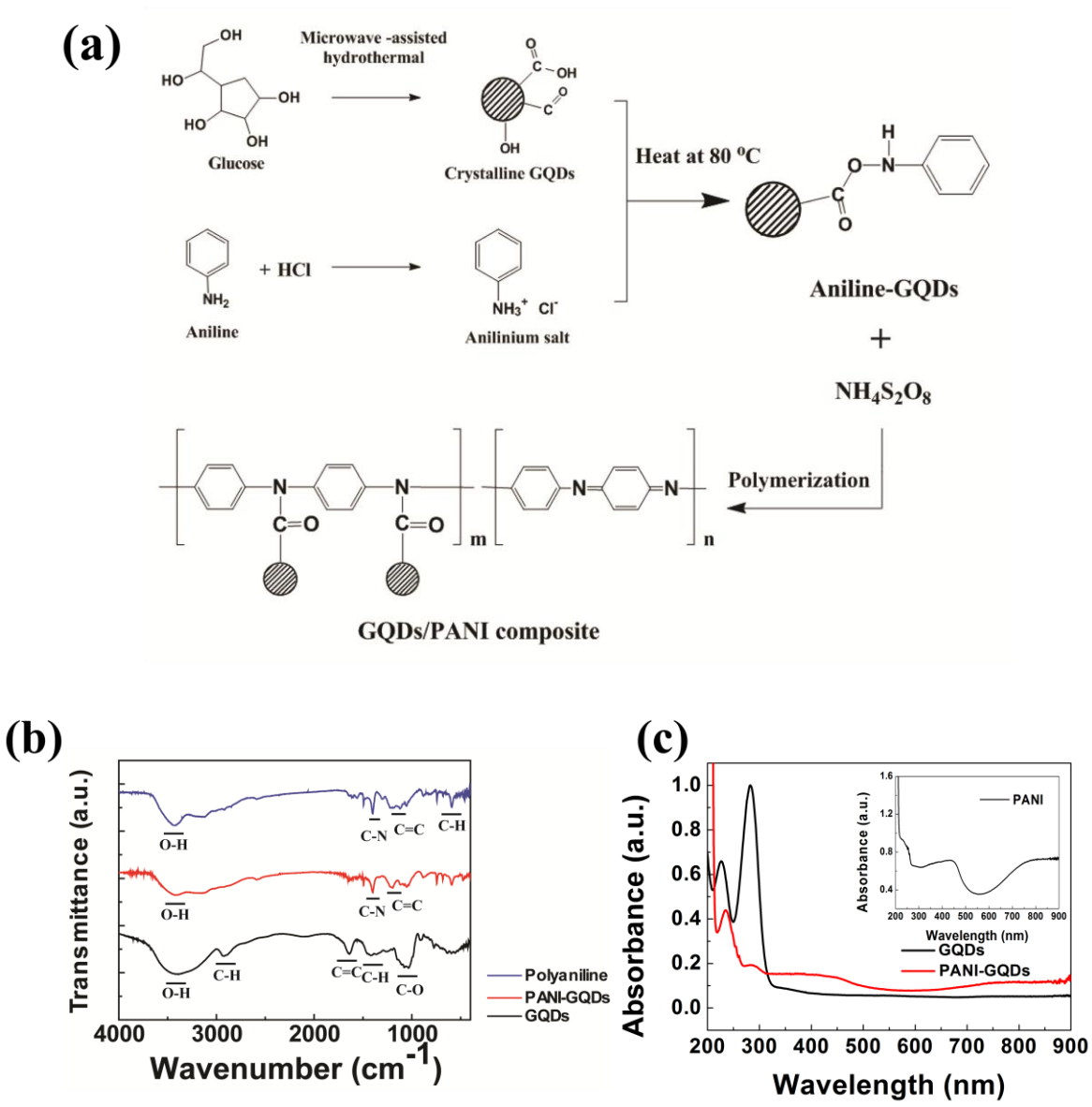

Figure 6.1 (a) Schematic diagram for the preparation of the PANI-GQD composite. (b) FT-IR spectra of the PANI, PANI-GQDs and GQDs. The GQDs was fabricated under the reaction pressure of 165 psi. (c) UV-Vis absorbance of the GQDs, and PANI-GQDs. The inset shows the absorbance of pure PANI.

We performed XPS on the samples to determine the surface composition and bonding of the PANI-GQD, as shown in Figure 6.2. The survey XPS of the

composite is mainly dominated by the signals of C, O and N. The measured C1s spectrum of the PANI-GQD can be fitted with five components, such as 284.5 eV (sp^2 bonded carbon), 285.3 eV (sp^3 bonded carbon), 286.5 eV (C-OH group), 287.1 eV (C-O-C group) and 288.1 eV (C=O group). For N1s spectrum of the composite, the curve can be deconvoluted into three components, which are 399.5 eV (pyridinic N), 401.0 eV (pyrrolic N) and 402.1 eV (graphitic N). The C/O and C/N atomic ratio for the PANI-GQD is 2.31 and 7.75 respectively.

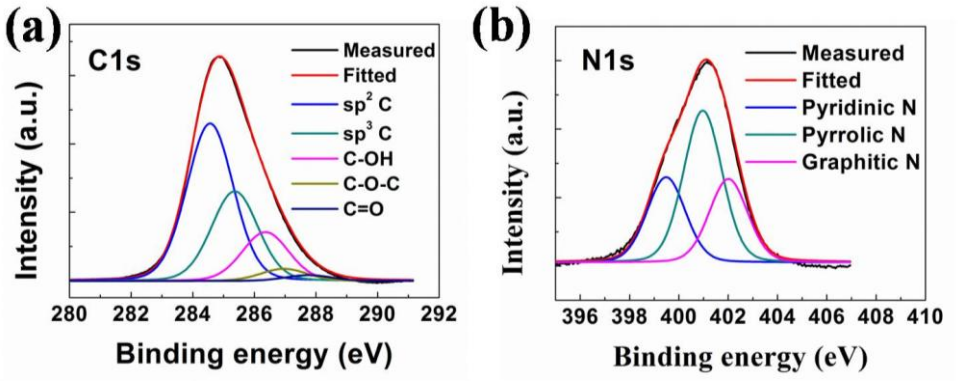

Figure 6.2 C1s XPS spectrum of (a) PANI-GQD. (b) N1s spectrum of the PANI-GQD.

Figure 6.3 shows the typical TEM images of the PANI-GQD dispersed on the copper grid. The results depict an almost uniform distribution of GQDs in the polymer matrix. Furthermore, the shape of the GQDs in the composite become irregular compared with the as-prepared GQDs, probably owing to the surface modification of the GQDs from chemical reaction between the functional groups located at the GQDs surface and polymer matrix.

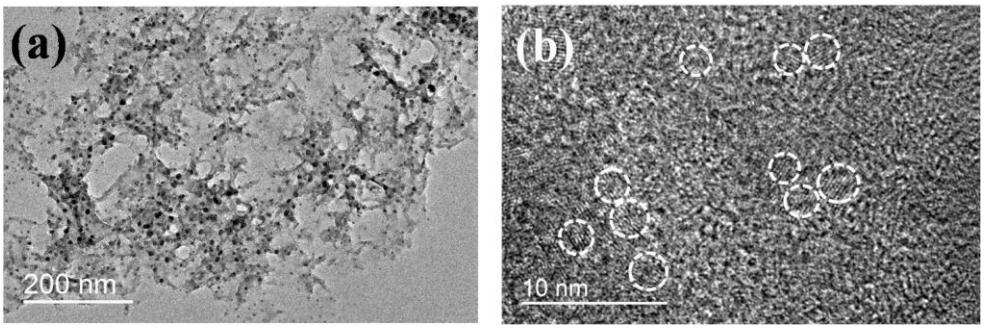

Figure 6.3 (a) Low-resolution and (b) high-resolution TEM images of the PANI-GQD composite respectively.

The PL spectra of the GQDs and PANI-GQD composites are shown in Figure 6.4. The excitation wavelength is 365 nm. For the GQDs with the diameter of 3.2 nm, the PL peak position of the GQDs is 454 nm. The PL emission peak is shifted to 489 nm after the functionalization of polyaniline with a mole number of 1 mmol. Since the size of the as-received GQDs and GQDs in PANI are similar; the redshift behavior is primarily attributed to aniline functionalization. We hypothesize that the aniline functional groups (amine group, -NH) can contribute to the electron donation from the amine group to the GQDs based on induced electron withdrawal, making π-conjugated system more electrophilic [116]. In the view of organic chemistry, since the GQD has large π-conjugated system, the electron donating group can be excited to the aromatic rings to form p-π conjugated system, thus enlarging the π-conjugated system [116]. The strong orbital interaction between aniline and π-conjugated system elevates the primary HOMO to a higher energy orbit [117]. To support this hypothesize, we varied the concentration of PANI to observe the PL shifts of the composites. The emission wavelength is shifted from 489 to 515 nm when the mole number increases from 1 to 5 mmol. The increased amount of amine group would enhance electron

delocalization densities, resulting in a much narrower optical band gap.

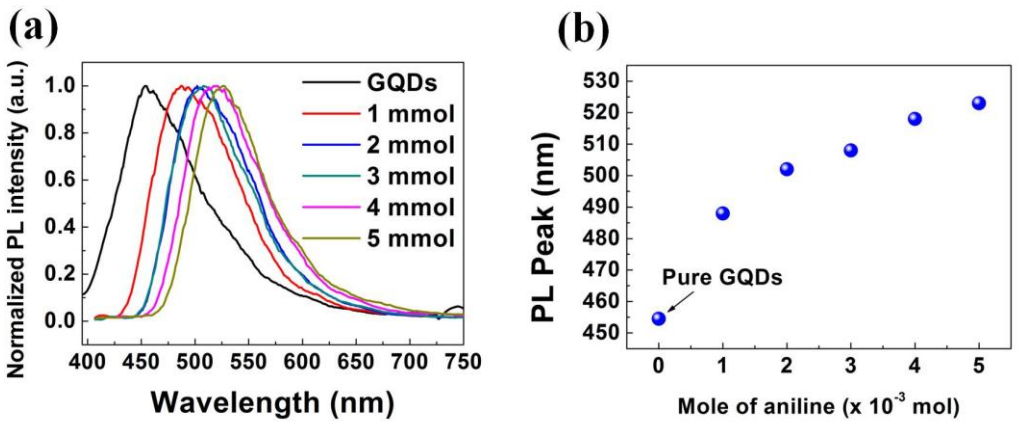

Figure 6.4 (a) Photoluminescence (PL) spectra of the PANI-GQDs with various moles of aniline. (b) The dependence of the PL emission on mole number of aniline.

Since the GQDs were shown to exhibit excitation dependent PL emission in some previous works [113, 118], a detailed PL measurement for the PANI-GQD composite was performed at different excitation wavelengths, as shown in Figure 6.5. The excitation wavelength was adjusted from 330 nm to 470 nm. Figure 6.5 (g) shows the overall summary of the PL emission of the composites with various excitation wavelengths. For the parent GQDs, The PL shifts from 440 nm to 554 nm when the excitation wavelength changed from 330 nm to 470 nm. With regard to the mole number of PANI, all the composites also show excitation-dependent emission which has a similar trend with the GQDs. The phenomenon of the excitation dependent emission in the GQDs and PANI-GQDs could be related to the surface states located at the GQD surface which will be discussed later.

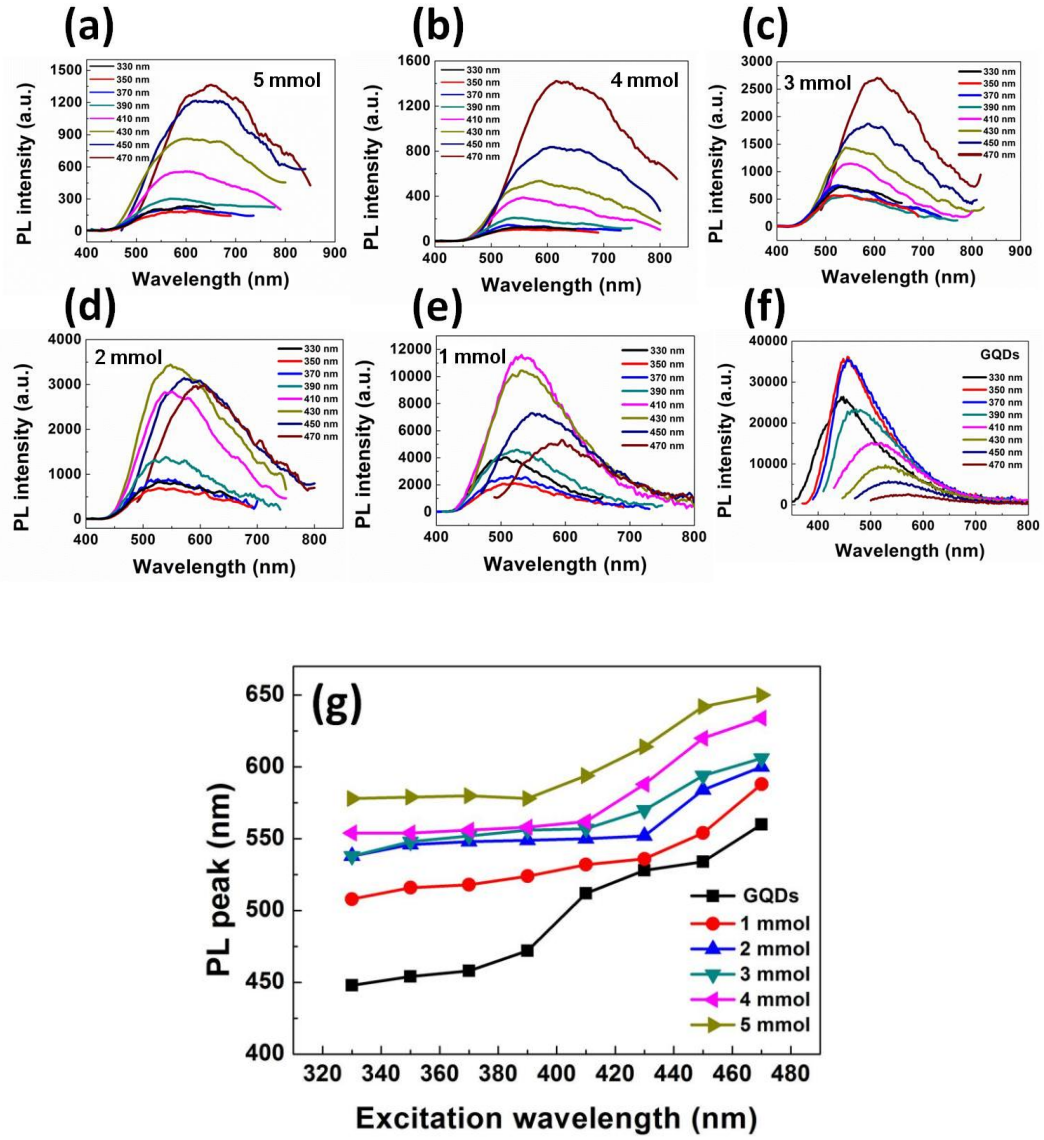

Figure 6.5 The excitation dependent PL emission with (a-f) different mole number of aniline. (g) A summary of the excitation dependent PL.

The Au/PANI-GQDs/ITO sandwich-structure device was prepared in order to study the electrical transport properties of the composite. The schematic diagram of the device is shown in the inset of Figure 6.6 (a). A nonlinear response of the PANI-GQD composite with significant hysteresis was observed, while the pure

PANI exhibits a linear current-voltage relationship as shown in Figure 6.6 (a) and (b), respectively. From the results shown, the electrical hysteresis behavior is reproducible by varying the maximum sweeping voltage, but independent on the sweep direction (either in clockwise or anti-clockwise direction). The formation of the hysteresis loop in both positive and negative bias voltage shows a characteristic memory phenomenon.

The I-V characteristics of the composites varied with the concentration of the PANI contained in the composite is shown in Figure 6.6 (c). The hysteresis with large amount of PANI is less pronounced. We also studied the effects of the size of the GQDs on the electrical characteristics in the composites (Figure 6.6 (d)). It is noted that the increase of the GQD size would lead to a decrease in the conductivity, and the hysteresis loop would also become smaller. The presence of the GQDs with various sizes may modulate the conduction paths.

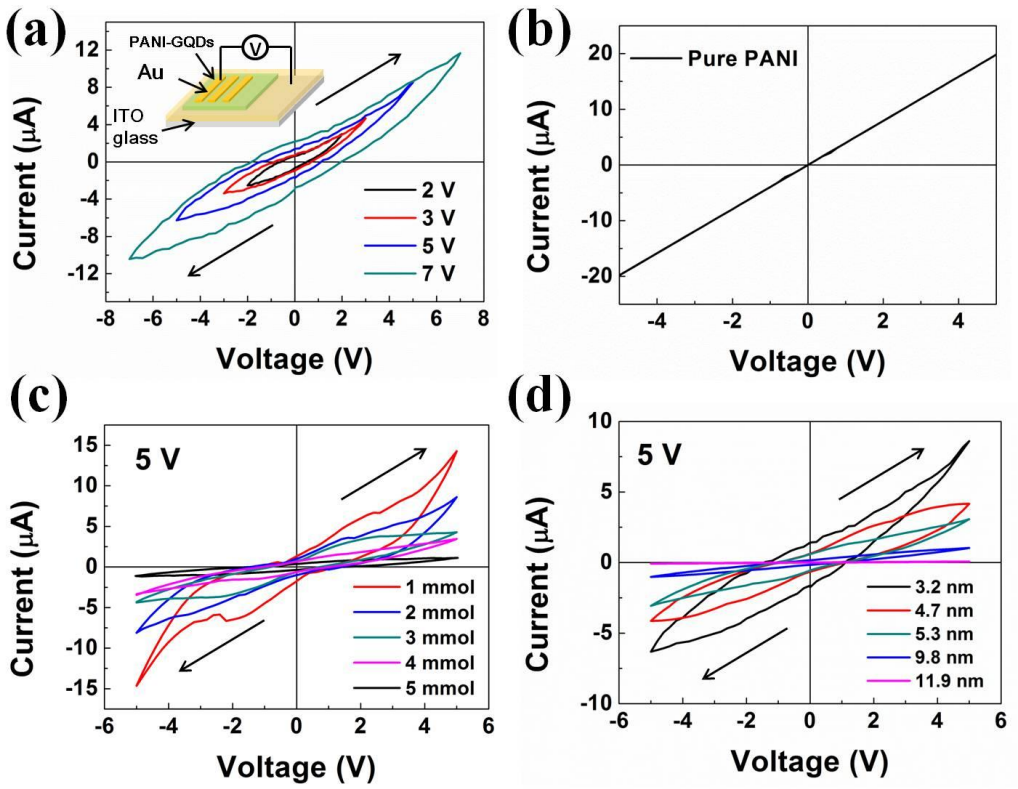

Figure 6.6 (a) Hysteresis behavior of the Au/PANI-GQD/ITO structure under different voltages. The inset depicts the device structure. (b) Linear relationship of the current-voltage characteristics of PANI. Hysteresis loops measured at (c) various moles of aniline and (d) sizes of the GQDs respectively. All the hysteresis behaviors were measured in clockwise direction with respect to the voltage.

The area within the hysteresis loop as a function of applied bias voltage, diameter of GQDs and content of PANI are depicted in Figures 6.7 (a) and (b). The area within the hysteresis loop is equivalent to the energy stored in the composite film. The hysteresis loop enlarged with increasing bias voltage amplitude, which can be explained by voltage induced conformational changes in the polymer structure [119] resulted from stronger detrapping and spartial distribution of charges at

higher voltage amplitude.

As demonstrated above, our GQDs consists of C=C core, O and H related functional groups at the surface. These functional groups, including C-OH, C-H, C-O, at the surface form "surface states" located at the energy level between π and π^* states of C=C. The surface states energy level can be estimated by the energy difference between the intrinsic absorption energy at 228 nm (5.44 eV) and the surface state absorption energy at 282 nm (4.40 eV). Thus, the surface states level is located at ~ 1.0 eV above π energy level of the GQDs [113]. The functional groups have various energy levels, therefore resulting in different emissive traps. When a certain excitation wavelength illuminates the GQDs, the emission is dominated by the surface state emission trap. However, the intrinsic absorption for PANI-GQD composites is shifted to 236 nm (5.25 eV) and this changes the location of the surface states, which become ~ 0.85 eV above π energy level (Figure 6.7 (c)). This makes easier for the charges to tunnel via the surface states. Hence, the surface states in the composite serves not only as various emission traps, but also as 'charge trapping centers'. Variations in surface states are expected as the electron delocalization densities changes as a result of changing PANI concentration. Consequently, it results in the change of the hysteresis behavior. The surface states induced by the functional groups plays an important role in both the tunable emission and hysteresis conducting behaviors of the PANI-GQDs composite.

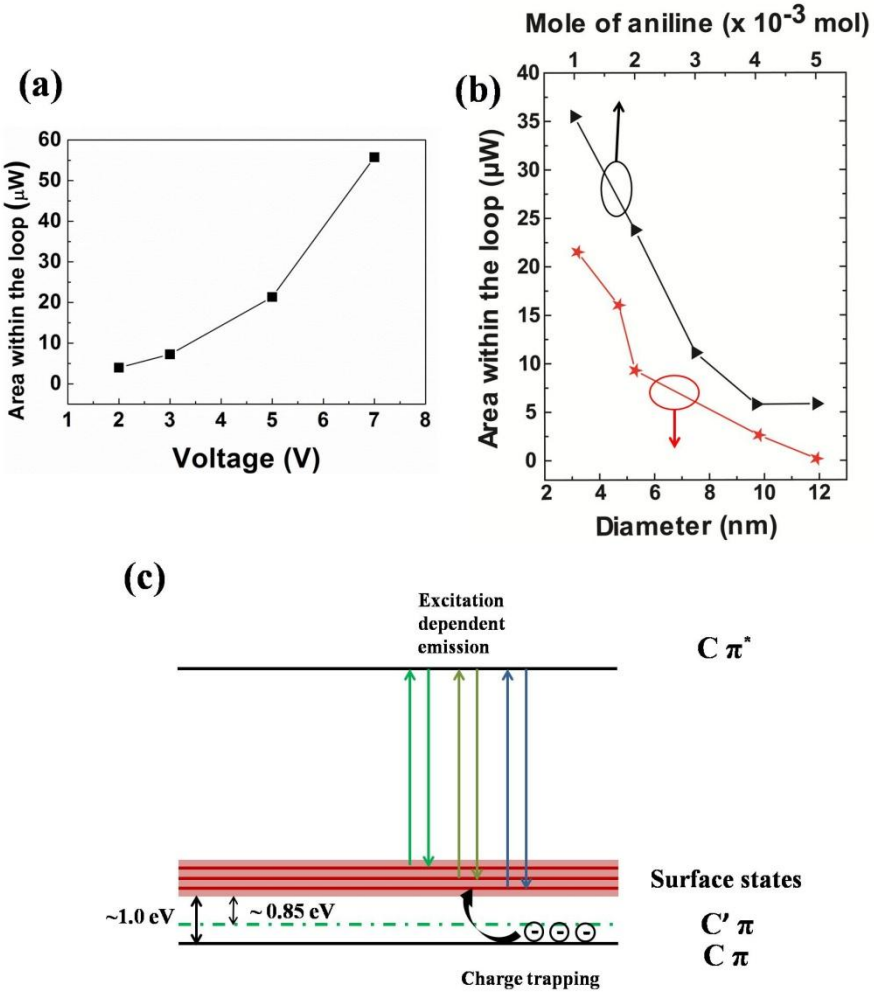

Figure 6.7 Plot of the area within the hysteresis loops as a function of (a) biased voltage, (b) mole number of aniline and diameter of the GQDs. (c) Schematic diagram of the energy level of the GQDs. The dash line (C'π) indicates the new intrinsic absorption of the PANI-GQD.

6.4 *Summary*

In summary, we have demonstrated the tunable PL and hysteresis behavior for GQDs embedded in PANI matrix. The PL redshift in the composite is attributed to π-conjugated system interaction between GQDs and PANI. The electrical measurements show a stable clockwise hysteresis loops under both forward and

reverse bias in I-V characteristics. The conductivity and hysteresis behavior can be tuned by changing the amounts of PANI and sizes of the GQDs. The controllable electrical and optical properties in the composite films are explained by the charge trapping sites located at the surface states induced by the functional groups. This work may open a wide range of application for GQD composite based devices.

Chapter 7 N-doping of GQDs

7.1 *Introduction*

Doping carbon materials with heteroatoms can effectively tune their intrinsic properties including electronic characteristics and chemical features. [120, 121] Among those heteroatoms, nitrogen (N) atom has been widely used for chemical doping of carbon nanomaterials. For instance, N doped carbon nanotubes (N-CNTs) showed highly effective electrocatalytic activities for the oxygen reduction reaction [122, 123]. Similarly, doping of GQDs with N atoms could effectively tune the band gap to introduce new properties for device applications. Nitrogen-doped graphene quantum dots (N-GQDs) can be prepared by various methods such as hydrothermal, electrochemical, organic synthesis and self-catalysis [43, 56, 124, 125]. The electrocatalystic activity [43, 124], tunable luminescence [56] and biocompatible application [56] have been demonstrated. In this chapter, it is found that the as-prepared N-GQDs show good fluorescent properties. They also have strong tunable luminescence from excitation of ultraviolet to visible range. Most interestingly, our N-GQDs exhibited two-photon luminescence which may find potential application in bioimaging or energy collection.

Previous chapters have already mentioned that the GQDs exhibited wavelength dependent luminescence where the emission shifted as the excitation wavelength changed. A single GQD particle contains multiple emissive states leading to the observation of excitation wavelength dependent emission in bulk samples. However, previous report of the single particle fluorescence of carbon nanodots with size ranged from 3 to 8 nm showed that isolated single GQDs did not

exhibit fluorescence at multiple wavelength but showed mutichromophoric behavior, which suggested that separate particles might be responsible for the emission at various excitation wavelengths rather than a single particle emitting at multiple wavelengths [126]. Single particle measurement allows the photoselection of a fraction of GQDs with similar properties. Here we utilize single particle fluorescence technique to characterize the luminescence properties of undoped and N-GQDs with NIR emission.

7.2 *Experimental*

The two-photon luminescence measurement has been described in chapter 3. For single particle fluorescent, the undoped and N-GQDs were immobilized on a cleaned glass coverslip by spiking a nano-molar concentration of the N-GQDs in poly vinyl alcohol (PVA) and spin coating on the coverslip. PVA solution (1 g/ml) was prepared in PBS buffer at pH 7.5. Microscope coverslips were cleaned by immersing in NaOH (5 Mol) for about 30 minutes. Before use coverslips were washed thoroughly in ultrapure water, rinsed in ethanol and dried with filtered nitrogen gas.

7.3 *Results and discussion*

7.3.1 *Two-photon luminescence*

The TEM image of the N-GQDs is shown in Fig. 7.1 (a). The prepared N-GQDs show monodispersed distribution. The HRTEM image, as shown in Fig. 7.1 (b) reveals high crystallinity of the N-GQDs. The corresponding selected area Fourier transform (FFT) image is shown in the inset of Fig. 7.1 (b), revealing the lattice fringes of the [110] and [1$\bar{1}$0] planes of graphite. The line profile analyze of the diffraction fringe of the N-GQDs is shown in Fig. 7.1 (c). The distance

between the lattice fringes is 0.23 nm which is close to that of bulk graphite. It is worth noting that the in-plane lattice spacing (0.23 nm) is slightly larger than that of bulk graphite (0.21 nm), probably due to the introduction of N atoms into the hexagonal carbon matrix [127]. The size distribution of the N-GQDs obeys Gaussian distribution (Fig. 7.1(d)). The most probable size is 5.9 nm with a full width at half maximum (FWHM) of 1.64 nm. Electron energy loss spectroscopy (EELS) is used to characterize the chemical composition and structure of the N-GQDs, as shown in Fig. 7.1 (e). There are four obvious peaks located at 285 eV, 296 eV, 401 eV and 408 eV. The first two peaks (285 and 296 eV) are attributed to the K-edges of C, corresponding to $1s \rightarrow \pi^*$ and $1s \rightarrow \sigma^*$ respectively. The latter peaks (401 and 408 eV) correspond to K-edges of N which associate with $1s \rightarrow \pi^*$ and $1s \rightarrow \sigma^*$ of C=N respectively [128]. The N/C atomic ratio of the N-GQDs is found to be 6.28%.

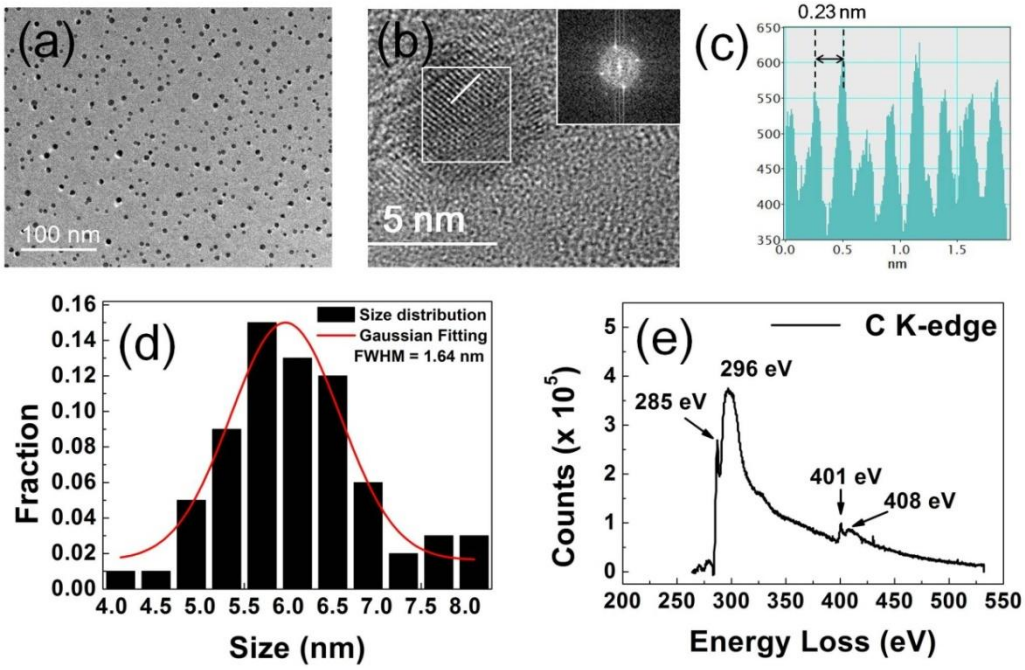

Figure 7.1 (a) TEM image of the N-GQDs assembled on Cu grid coated with ultrathin amorphous carbon film. (b) HRTEM image of the N-GQDs. Inset: The fast Fourier transform (FFT) image of a selected area (white square). (c) The line profile analyses of the diffraction fringes. The lattice parameter is 0.23 nm. (d) Size distribution of the N-GQDs. (e) EELS spectrum of the N-GQDs.

The UV-Vis absorbance spectrum of the N-GQDs is shown in Fig. 7.2 (a). There are three UV absorption peaks located at 215 nm, 272 nm and 302 nm. These peaks are associated with the electron transitions from π (or n) to π* of C=C, C=N and C=O respectively [127]. Comparing with the UV-Vis absorption of undoped GQDs (Fig. 6.2 (b)), the GQDs exhibit two absorption peaks at 228 nm ($\pi \rightarrow \pi^*$ of C=C) and 283 nm ($n \rightarrow \pi^*$ of C=O).

The excitation-dependent photoluminescence (PL) for the N-GQDs is shown in Fig. 7.2 (c). Similar to conventional carbon-based quantum dots [11, 129], the

emission wavelength is dependent on the excitation wavelength. An emission peak at 520 nm is observed when the sample is excited by 350 nm. When the excitation wavelength changed from 350 to 520 nm, the PL peak shifted from 520 to 593 nm. As shown in Fig 7.2 (d), the emission wavelength increases with the excitation in a linear relationship. The tunable PL can be explained in terms of surface states formed by the functional groups [130] at the surface of the N-GQDs. Briefly, the functional groups have different energy levels which results in a series of emissive traps. The surface state emissive trap dominates the emission at a certain wavelength. By comparing with the PL spectra of the undoped GQDs excited by various wavelengths, the emission peak of the N-GQDs shift to longer wavelength [6]. It is believed that N doping dominates the shift of the emission. The quantum yield (QY) of the N-GQDs was determined to be 8.4 %, which is comparable to undoped GQDs prepared by other methods [11, 128, 129,131].

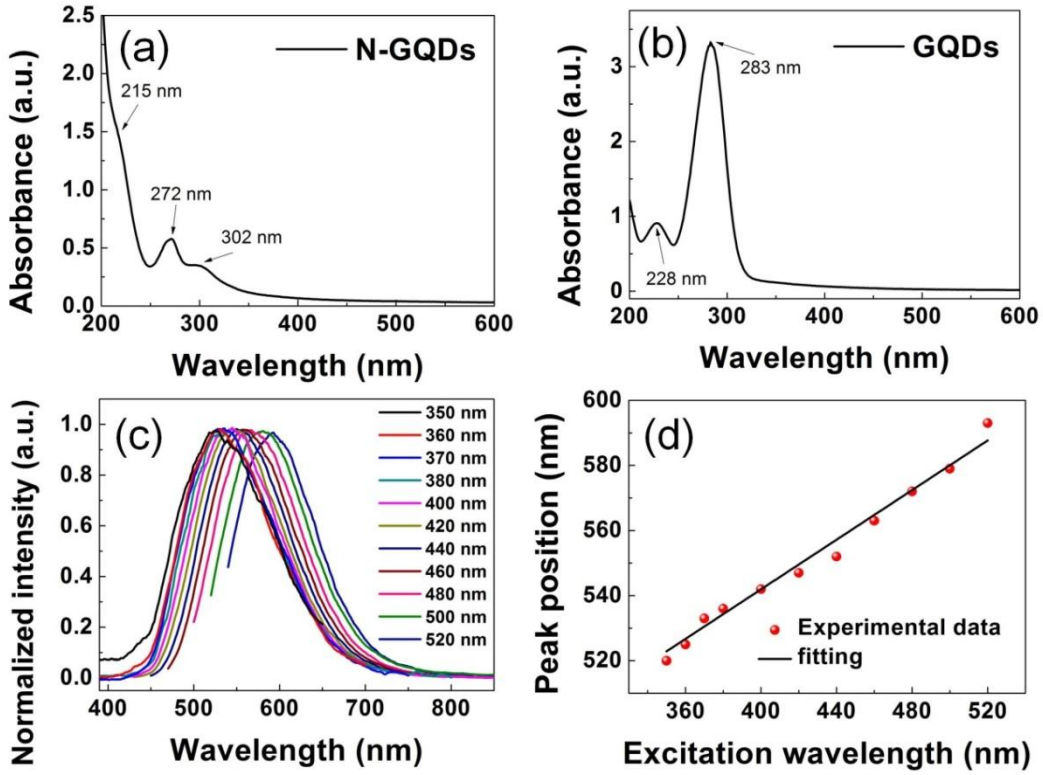

Figure 7.2 UV-Vis absorbance of the (a) N-GQDs and (b) undoped GQDs. (c) PL spectra of the N-GQDs excited by various wavelengths. (d). The linear relationship between the emission and excitation wavelength of the N-GQDs.

Apart from the strong downconversion PL features, the N-GQDs also exhibit upconversion PL properties. As shown in Fig. 7.3 (a), when the excitation wavelength changes from 700 to 950 nm, the upconverted emission peak shifts from 472 to 596 nm. In addition, it is found that the emission peak is generally broad and dependent on excitation wavelength. The strongest PL emission (FWHM ~ 150 nm) is located at 517 nm when the excitation wavelength is 800 nm. The upconversion properties of N-GQDs may be beneficial to energy transfer component in photocatalyst design [132] and bioimaging [13]. The upconversion PL can be generally explained by two mechanisms, the

multiphoton active process and anti-Stokes PL. The former is associated with the relationship between the emission intensity and input pump power, while the latter is related to the energy difference (ΔE) between excitation and emission wavelengths. As proposed by Hoffmann [133], the value of ΔE should be kept constant and less than 1.5 eV. To explore the upconversion mechanism of our N-GQDs, the shifting between the energy of upconverted emission (E_m) and excitation (E_x) is plotted in Fig. 7.3 (b). The linear relationship between E_m and E_x appears at the plot with a fitting function. The value of ΔE in N-GQDs is ranged from 0.7 to 0.9 eV, which does not remain constant. In addition, the power-dependent emission of the N-GQDs is studied by tuning the laser pump power (Fig. 6.3 (c)). The N-GQDs were excited by the wavelength of 900 nm with the laser power changed from 835 to 1670 mW. As the power increases, the upconverted emission intensity of the N-GQDs increases without any peak shift. The inset shows the quadratic relationship obviously between the intensity and laser power. These results suggest the two-photon excitation is responsible for the upconversion luminescence [134]. The emission with various N/C atomic ratios of the N-GQDs excited by 900 nm is shown in Fig. 7.3 (d). The N/C ratio of the N-GQDs is determined by EELS. At low N/C ratio, there is almost no emission. When the N/C ratio increases, the emission intensity also increases. The result shows that N doping play an important role on two-photon luminescence.

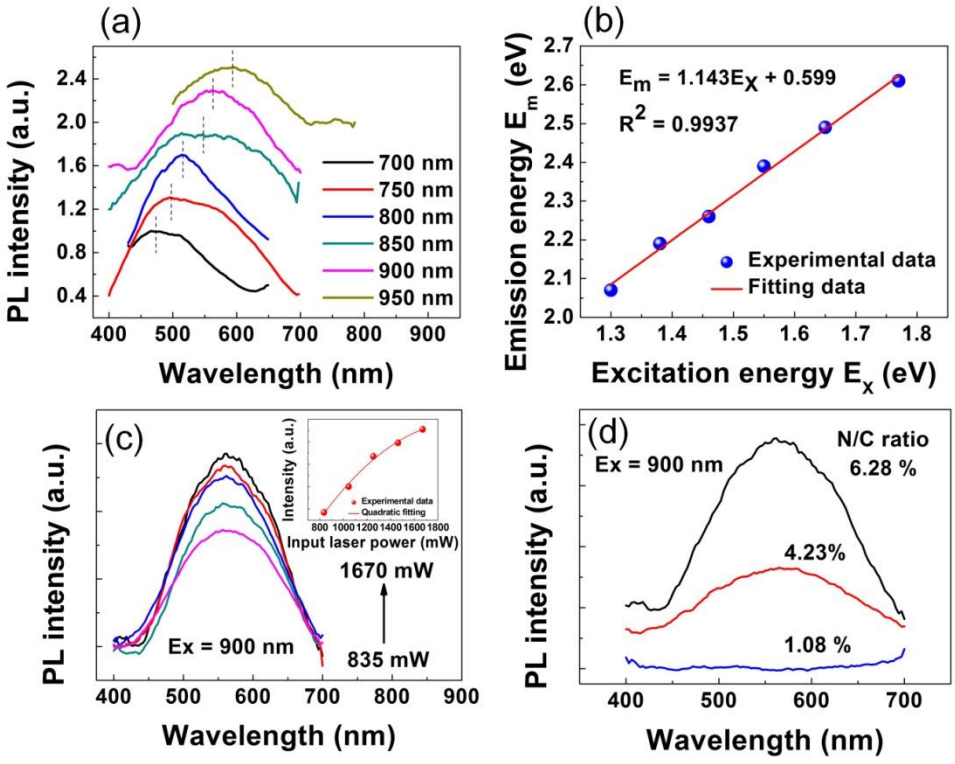

Figure 7.3 Two-photon PL spectra of the N-GQDs. (b) The energy of the emission light as a function of the excitation light. (c) The emission intensity with various input pump power. The excitation wavelength is 900 nm. Inset: The quadratic relationship of the obtained PL intensity of the N-GQDs with the excitation power. (d) The PL spectra with various N/C atomic ratios at the excitation of 900 nm.

The luminescence of the N-GQDs may originate from the π –π electron transition since the N-GQDs has large π conjugated system. Furthermore, the lone pair electrons from the strong electron donating group NH_3 which is doped to the aromatic ring of N-GQDs, can be excited to the aromatic rings to form the p–π conjugation, further enlarging the π-conjugated system. [135] .The strong orbital interaction between NH_3 bonding and π-conjugated system of the N-GQDs elevates the primary HOMO to a higher orbit [117]. This results in facilitating the

charge transfer and enhancing the two-photon excitation. Hence, strong two-photon induced luminescence can be observed.

7.3.2 *Single-particle fluorescence*

To determine the size effect on the photophysical properties of undoped and N-GQDs, we isolated particles in a thin film of polyvinyl alcohol (PVA) on a glass cover slip. We then imaged individual particles using 488 nm, 561 nm, and 640 nm excitation. At bulk concentrations, solution based measurements with 488 nm excitation showed high levels of fluorescence. However, when samples were diluted to single particle levels no signal was detected above the background level indicating the individual particles are not bright enough to be observed with 488 nm excitation. However, with both 561 nm and 640 nm excitation individual molecules were clearly visible. To determine if the same particles exhibited fluorescence at both 561 nm and 640 nm excitation we imaged identical fields of view with both wavelengths for all species of GQDs. Overlaying the images taken at 561 and 640 nm excitation showed no overlap between particles from these two channels (Fig. 7.4). This indicated that no particle possessed chromophores which can be excited by both 561 nm and 640 nm within the same particle.

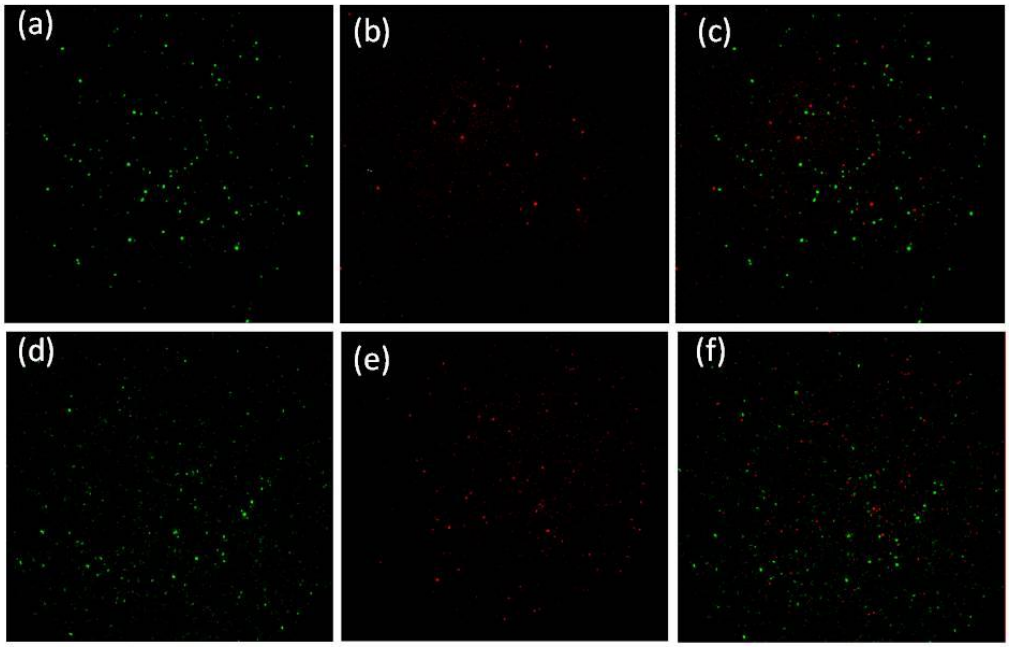

Figure 7.4 (a) Wide field fluorescence image of non-doped GQDs (3.0 nm average size) with 561 nm excitation. (b) The same field of view using 640 nm excitation. (c) An overlay of (a) and (b). (d) Wide field fluorescence image of N-doped GQDs (3.4 nm average size) with 561 nm excitation. (e) The same field of view using 640 nm excitation. (f) An overlay of (d) and (e).

We performed experiments to determine the relative population of red (561 nm excitation) particles compared to the NIR (640 nm excitation) particles for each species. Within an electron multiplying charge coupled device (EMCCD) field of view of isolated particles we counted the number of each species. In all samples, there was always fewer NIR (660 nm to 1000 nm) emitting particles than red (607 ±27 nm) emitting particles. For non-doped samples, there was always fewer NIR (660 nm to 1000 nm) emitting particles than red (607 ±27 nm) emitting particles. The ratio of NIR to red emitting particles decreases from ~0.45 to 0.14

when the average size of the particles increases from 3 nm to 11 nm, as shown in Fig. 7.5.

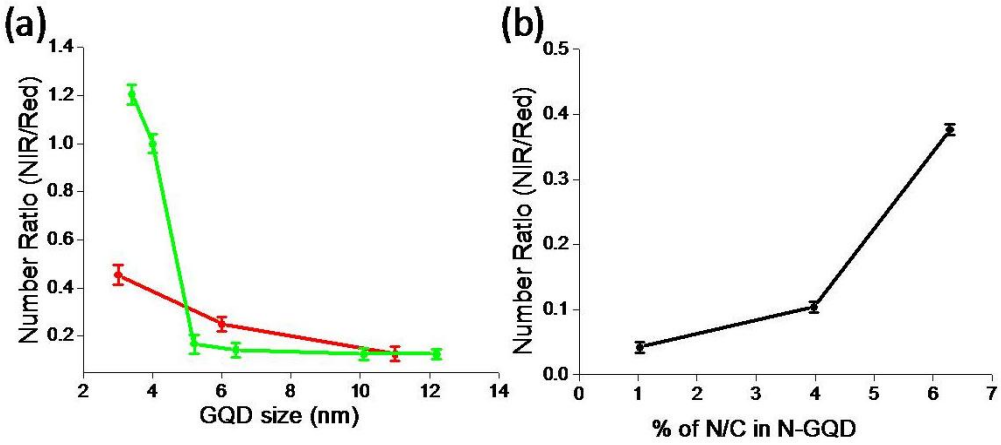

Figure 7.5 Variation of the ratio of the number of NIR to red emitting particles. (a) The variation of the number of NIR emitting particles (640 nm excitation) to red emitting particles (561 nm excitation) for non-doped and N-doped GQDs. with the size. The red line represents non-doped GQDs and the green line N-doped GQDs. (b)The variation of the ratio with the value of N/C in N-GQDs (average size of 6 nm).

The distribution of particle populations in the N-doped GQDs is more striking. The ratio of the number of NIR to red emitting particles decreases from 1.2 to 0.17 when the average size increases from 3.4 to 5.2 nm. All the doped particles larger than 5.2 nm showed a similar ratio of ~0.17. The NIR emitting species only becomes the most abundant for small doped particles. These results suggested that the observed photophysical properties could be related to the level of doping for each particle species. Subsequent tests to determine the percent dopant using electron EELS showed that the percent doping measured as N/C

atomic ratio increases from 5% to 7% as the particle size decreases (Fig. 7.6). This suggests that the observed changes in relative number of NIR emitting particles might be related to the dopant percent rather than the size. The significant effect of nitrogen dopant percentage on NIR emitting particles are consistent with previous ensemble measurements, reporting that higher nitrogen content shifts GQD emission to the red.

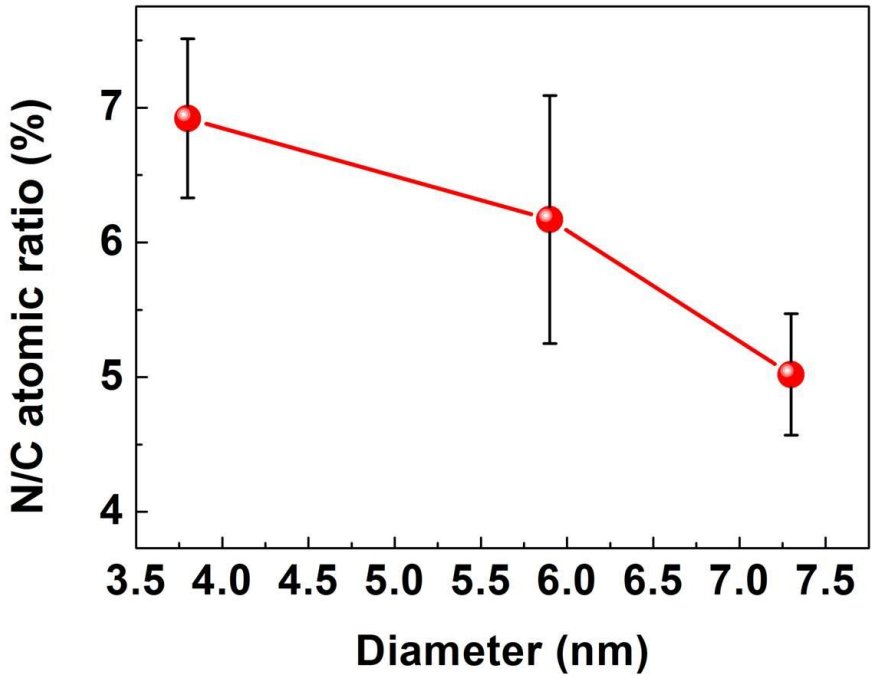

Figure 7.6 Variation of N/C percentage ratio of N-GQDs with their average size as measured by EELS.

To determine if the observed trends in the NIR emitting particles correlate to the amount of dopant in the N-GQDs, we prepared three N-GQDs with the same diameter (~ 6 nm) but with varying amounts of nitrogen dopant. These N-GQDs had a N/C ratio as measured by EELS of 1.03%, 3.98%, and 6.28%. Single particle fluorescence imaging of these particles shows that the relative population

of NIR (640 nm excitation) emitting particles compared to red (561 nm excitation) emitting particles increases with an increase of the dopant content (Fig. 7.5 (b)). The value increases from 0.04 to 0.38 as the N/C ratio increases from 1.03% to 6.28%. Thus, the increase in nitrogen content of particles with the same diameter resulted in an increase in the ratio of NIR emitting particles to red emitting particles. This suggests that the higher proportion of NIR emitting particles observed in smaller N-GQDs (~3 nm) compared to the larger ones (~12 nm) is, at least partially, a consequence of doping levels. This suggests the apparent size dependence observed in Fig. 6.5 is related to the level of dopant. In this circumstance, it is important to take into account that the smaller particles have a higher surface area per unit volume of GQD compared to larger particles and the doping of nanoparticles is primarily a function of the surface area. Thus, the N atom content with respect to carbon content would be highest in the smaller particles. This suggests that doping is size dependent, and that dopant levels play a prominent role in NIR emission. It should be noted that we are measuring only those particles with sufficient intensities to be visible at the single particle level. It is possible that there are particles with insufficient intensity to be counted. Thus, the changes we observe could be either from changes in the distribution of the fluorophores or from changes in the intensity of the fluorescence from a particular emissive species.

We suggest from the results above that the NIR emission is at least partially size dependent. However, we observe the largest fraction of NIR emitting particles for 3.4-5.2 nm N doped GQDs. The smallest doped particles have a ratio of 1.2 (NIR to red). This substantial increase in the fraction of NIR particles strongly suggests a correlation with the percent doping and is supported by the

observation of N-GQDs with different N/C ratios (Fig. 7.5 (b)). As the size of a particle increases, the amount of doped N atoms relative to carbon content in GQDs decreases as the doping reaction rate increases with increased surface area of the nanoparticle. Therefore, the percentage of N/C content is largest for 3.4 nm N-GQDs.

7.4 *Summary*

In conclusion, we have demonstrated a "one-pot" microwave-assisted hydrothermal synthesis of N-GQDs. The N-GQDs exhibited excellent optical properties with tunable and two-photon induced luminescence. The N-GQDs may provide a new type of fluorescence and upconversion material for applications in bioscience and energy technology. They may also open an opportunity for application of graphene-based materials to other fields.

We have also explored the single-particle fluorescence of both GQDs and N-GQDs with average size ranged from ~3 to ~ 12 nm and various N/C atomic ratios. We observed moderate size dependent properties, but doping plays an important role on the photophysical properties. The NIR emission of N-GQDs was significantly dependent on the dopant concentration.

Chapter 8 Conclusion and Future Prospect

8.1 *Conclusion*

In conclusion, GQDs have been successfully synthesized by microwave-assisted hydrothermal technique. It is found that the structural and optical properties of the GQDs can be changed by varying the reaction time and pressure. The PL spectrum of the GQDs shows excitation wavelength dependent emission. The PL peak is red-shift when increasing the excitation wavelength. Utilizing their excellent luminescent properties, we fabricate GQDs-agar composite and use as a light conversion material on the blue LED. The CRI and CCT of the WLED were determined as 72 and 5532 K, which corresponding to cool white colour. The light conversion efficiency of the WLED is ~ 61 % under 20 mA of applied current.

The electrical hysteresis of PANI-GQD composite has been investigated. The composite is prepared by chemical oxidation polymerization. The PL emission is found to be tuned by varying the mole concentration of PANI and sizes of the GQDs. In order to study the electrical transport of the composite film, the Au/PANI-GQD/ITO sandwich device is demonstrated. Tunable electrical hysteresis can be observed under different mole concentration of PANI and size of the GQDs. Both the tunable PL and electrical hysteresis behavior were attributed to the surface states of the GQDs.

The downconversion and two-photon luminescence of N-GQDs have been demonstrated respectively. It is shown that both the downconversion and two-

photon emission exhibit excitation wavelength dependent emission. For two-photon luminescence, the quadratic relationship between the emission intensity and input laser power of the N-GQDs can be reached. The two-photon emission intensity can be varied by different N/C atomic ratios. It is believed that the N doping is critical for two-photon luminescence.

The fluorescent properties of undoped and N-GQDs have been investigated at single particle level. It was shown that N-GQDs exhibited larger proportion of particles with NIR emission by comparing with undoped GQDs. Both undoped and N-GQDs showed size dependent photophysical properties. It is suggested that doping GQDs results in significant changes in the NIR emissive properties.

8.2 *Future prospect*

Although our as-prepared GQDs show excellent optical properties, further works are required to explore their practical application. Some properties such as stability in atmosphere, product yield, the confusing PL mechanism, accurate control of lateral dimensions and quantum yield need to be further improved. By suitable doping and chemical exploitation, this may open the door to potential application ranging from data storage, bioimaging to energy collection.

References

[1] X. Y. Xu, R. Ray, Y. L. Gu, H. J. Ploehn, L. Gearheart, K. Raker and W. A. Scrivens, J. Am. Chem. Soc. 2004, 126, 12736-12737.

[2] K. S. Novoselov, A. K. Geim, S. V. Morozov, D. Jiang, Y. Zhang, S. V. Dubonos, I. V. Grigorieva and A. A. Firsov, Science, 2004, 306, 666–669.

[3] H. Brody, Nature, 2012, 483, S29.

[4] K. S. Novoselov, I. V. Grigorieva, L. Colombo, P. R. Gellert, M. G. Schwab and K. Kim, Nature, 2012, 490, 192-200.

[5] I. Jung, D. A. Dikin, R. D. Piner and R. S. Ruoff, Nano Lett. 2008, 8, 4283-4287.

[6] L. S. Li and X. Yan, J. Phys. Chem. Lett., 2010, 1, 2572–2576.

[7] L. L. Li, J. Ji, R. Fei, C. Z. Wang, Q. Lu, J. R. Zhang, L. P. Jiang and J. J. Zhu, Adv. Funct. Mater. 2012, 22, 2971–2979.

[8] X. Yan, X. Cui, B. Li and L. S. Li, Nano Lett., 2010, 10, 1869–1873.

[9] X. Zhou, Y. Zhang, C. Wang, X. Wu, Y. Yang, B. Zheng, H. Wu, S. Guo and J. Zhang, ACS Nano, 2012, 6, 6592–6599.

[10] D. Y. Pan, J. C. Zhang, Z. Li and M. H. Wu, Adv. Mater., 2010, 22, 734–738.

[11] L. Tang, R. Ji, X. Cao, J. Lin, H. Jiang, X. Li, K. S. Teng, C. M. Luk, S. Zeng, J. Hao and S. P. Lau, ACS Nano, 2012, 5102–5110.

[12] S. Zhuo, M. Shao and S. T. Lee, ACS Nano, 2012, 6, 1059– 1064.

[13] S. Zhu, J. Zhang, S. Tang, C. Qiao, L. Wang, H. Wang, X. Liu, B. Li, Y. Li, W. Yu, X. Wang, H. Sun and B. Yang, Adv. Funct. Mater. 2012, 22,

4732–4740.

[14] H. Razmi and R. Mohammad-Rezaei, Biosens. Bioelectron., 2013, 41, 498–504.

[15] H. Zhao, Y. Chang, M. Liu, S. Gao, H. Yu and X. Quan, Chem. Commun., 2013, 49, 234–236.

[16] S. Zhu, J. Zhang, C. Qiao, S. Tang, Y. Li, W. Yuan, B. Li, L. Tian, F. Liu, R. Hu, H. Gao, H. Wei, H. Zhang, H. Sun and B. Yang, Chem. Commun., 2011, 47, 6858–6860.

[17] Y. Dong, C. Chen, X. Zheng, L. Gao, Z. Cui, H. Yang, C. Guo, Y. Chi and C. M. Li, J. Mater. Chem., 2012, 22, 8764–8766.

[18] V. Gupta, N. Chaudhary, R. Srivastava, G. D. Sharma, R. Bhardwaj and S. Chand, J. Am. Chem. Soc., 2011, 133, 9960–9963.

[19] S. J. Yu, M. W. Kang, H. C. Chang, K. M. Chen and Y. C. Yu, J. Am. Chem. Soc., 2005, 127, 17604–17605.

[20] V. N. Mochalin and Y. Gogotsi, J. Am. Chem. Soc., 2009, 131, 4594–4595.

[21] S. Qu, X. Wang, Q. Lu, X. Liu and L. Wang, Angew. Chem. 2012, 124, 12381–12384.

[22] H. Li, Z. Kang, Y. Liu and S. T. Lee, J. Mater. Chem. 2012, 22, 24230–24253.

[23] S. N. Baker and G. A. Baker, Angew. Chem., Int. Ed., 2010, 49, 6726–6744.

[24] L. Cao, X. Wang, M. J. Meziani, F. Lu, H. Wang, P. G. Luo, Y. Lin, B. A. Harruff, L. M. Veca, D. Murray, S.-Y. Xie and Y.-P. Sun, J. Am. Chem. Soc., 2007, 129, 11318–11319.

[25] S. T. Yang, L. Cao, P. G. Luo, F. Lu, X. Wang, H. Wang, M. J. Meziani, Y. Liu, G. Qi and Y. P. Sun, J. Am. Chem. Soc., 2009, 131, 11308–11309.

[26] R. Liu, D. Wu, X. Feng and K. Muellen, J. Am. Chem. Soc. 2011, 133, 15221–15223.

[27] Z. Zhang, J. Zhang, N. Chen and L. Qu, Energy Environ. Sci., 2012, 5, 8869–8890.

[28] J. Shen, Y. Zhu, X. Yang, J. Zong, J. Zhang and C. Li, New J. Chem., 2012, 36, 97–101.

[29] L. A. Ponomarenko, F. Schedin, M. I. Katsnelson, R. Yang, E. W. Hill, K. S. Novoselov and A. K. Geim, Science, 2008, 320, 356–358.

[30] J. Shen, Y. Zhu, C. Chen, X. Yang and C. Li, Chem. Commun. 2011, 47, 2580–2582.

[31] J. Peng, W. Gao, B. K. Gupta, Z. Liu, R. Romero-Aburto,L. Ge, L. Song, L. B. Alemany, X. Zhan, G. Gao, S. A. Vithayathil, B. A. Kaipparettu, A. A. Marti, T. Hayashi, J.-J. Zhu and P. M. Ajayan, Nano Lett. 2012, 12, 844–849.

[32] Y. Li, Y. Hu, Y. Zhao, G. Shi, L. Deng, Y. Hou and L. Qu, Adv. Mater., 2011, 23, 776–780.

[33] M. Zhang, L. Bai, W. Shang, W. Xie, H. Ma, Y. Fu, D. Fang, H. Sun, L. Fan, M. Han, C. Liu and S. Yang, J. Mater. Chem. 2012, 22, 7461–7467.

[34] Y. Dong, J. Shao, C. Chen, H. Li, R. Wang, Y. Chi, X. Lin and G. Chen, Carbon, 2012, 50, 4738–4743.

[35] X. Yan, X. Cui and L. S. Li, J. Am. Chem. Soc., 2010, 132, 5944–5945.

[36] H. P. Liu, T. Ye, C. D. Mao, Angew. Chem. 2007, 119, 6593-6595.

[37] A. B. Bourlinos, A. Stassinopoulos, D. Anglos, R. Zboril, V. Georgakilas, E. P. Giannelis, Chem. Mater. 2008, 20, 4539-4541.

[38] J. Lu, P. S. E. Yeo, C. K. Gan, P. Wu and K. P. Loh, Nat. Nanotechnol. 2011, 6, 247–252.

[39] H. Zhu, X. L. Wang, Y. L. Li, Z. J. Wang, F. Wang, X. R. Yang, Chem. Commun. 2009, 5118-5120.

[40] D. B. Shinde and V. K. Pillai, Chem.–Eur. J., 2012, 18, 12522–12528.

[41] L. Lin and S. Zhang, Chem. Commun., 2012, 48, 10177–10179.

[42] S. Chen, J.-W. Liu, M. L. Chen, X. W. Chen and J. H. Wang, Chem. Commun., 2012, 48, 7637–7639.

[43] Y. Li, Y. Zhao, H. Cheng, Y. Hu, G. Shi, L. Dai and L. Qu, J. Am. Chem. Soc., 2011, 134, 15–18.

[44] D. B. Shinde and V. K. Pillai, Chem. -Eur. J. 2012, 18, 12522-12528.

[45] L. Zhang, Y. Xing, N. He, Y. Zhang, Z. Lu, J. Zhang and Z. Zhang, J. Nanosci. Nanotechnol., 2012, 12, 2924–2928.

[46] D. Pan, J. Zhang, Z. Li, C. Wu, X. Yan and M. Wu, Chem. Commun., 2010, 46, 3681–3683.

[47] H. Li, X. He, Y. Liu, H. Huang, S. Lian, S. T. Lee and Z. Kang, Carbon, 2011, 49, 605–609.

[48] J. Lu, J. X. Yang, J. Z. Wang, A. L. Lim, S. Wang and K. P. Loh, ACS Nano, 2009, 3, 2367–2375.

[49] H. X. Zhao, L. Q. Liu, Z. D. Liu, Y. Wang, X. J. Zhao and C. Z. Huang, Chem. Commun., 2011, 47, 2604–2606.

[50] Z. A. Qiao, Y. Wang, Y. Gao, H. Li, T. Dai, Y. Liu and Q. Huo, Chem.

Commun., 2010, 46, 8812–8814.

[51] H. Li, X. He, Z. Kang, H. Huang, Y. Liu, J. Liu, S. Lian, C. H. A. Tsang, X. Yang and S. T. Lee, Angew. Chem., Int. Ed., 2010, 49, 4430–4434.

[52] J. Zhou, C. Booker, R. Li, X. Zhou, T.-K. Sham, X. Sun and Z. Ding, J. Am. Chem. Soc., 2007, 129, 744–745.

[53] W. C. W. Chan and S. M. Nie, Science, 1998, 281, 2016–2018.

[54] X. Michalet, F. F. Pinaud, L. A. Bentolila, J. M. Tsay, S. Doose, J. J. Li, G. Sundaresan, A. M. Wu, S. S. Gambhir and S. Weiss, Science, 2005, 307, 538–544.

[55] A. M. Smith and S. Nie, Acc. Chem. Res. 2010, 43, 190–200.

[56] C. Hu, Y. Liu, Y. Yang, J. Cui, Z. Huang, Y. Wang, L. Yang, H. Wang, Y. Xiao and J. Rong, J. Mater. Chem. B, 2013, 1, 39–42.

[57] L. Bao, Z. L. Zhang, Z.-Q. Tian, L. Zhang, C. Liu, Y. Lin, B. Qi and D.-W. Pang, Adv. Mater. 2011, 23, 5801–5806.

[58] X. Yan, B. Li, X. Cui, Q. Wei, K. Tajima and L. S. Li, J. Phys. Chem. Lett. 2011, 2, 1119–1124.

[59] H. Tetsuka, R. Asahi, A. Nagoya, K. Okamoto, I. Tajima, R. Ohta and A. Okamoto, Adv. Mater., 2012, 24, 5333–5338.

[60] S. H. Jin, D. H. Kim, G. H. Jun, S. H. Hong, S. K. Jeon, ACS Nano, 2013, 7 (2), 1239.

[61] Z. Qian, J. Zhou, J. Chen, C. Wang, C. Chen and H. Feng, J. Mater. Chem., 2011, 21, 17635–17637.

[62] D. Qu, M. Zheng, P. Du, Y. Zhou, L. Zhang, D. Li, H. Q. Tan, Z. Zhao, Z. G. Xie and Z. Sun, Nanoscale, 2013, 5, 12272.

[63] K. Gong, F. Du, Z. Xia, M. Durstock and L. Dai, Science, 2009, 323, 760–764.

[64] K. Parvez, S. Yang, Y. Hernandez, A. Winter, A. Turchanin, X. Feng and K. M¨ullen, ACS Nano, 2012, 6, 9541–9550.

[65] S. H. Li, Y. Li, Jun Cao, J. Zhu, L. Fan, and X. Li, Anal. Chem. 2014, 86, 10201−10207.

[66] L.B. Tang, R. Ji, X. Li, G. Bai, C. P. Liu, J. H. Hao, J. Lin, H. Jiang, K. S. Teng, Z. Yang, and S. P. Lau, ACS Nano, 8, 6312-6320.

[67] X. Li, S. P. Lau, L. B. Tang,bc R. Ji and P. Yang, J. Mater. Chem. C, 2013, 1, 7308.

[68] J. R. Lill, E. S. Ingle, P. S. Liu, V. Pham, W. N. Sandoval, Mass Spectrom. Rev. 2007, 26, 657.

[69] C. O. Kappe, A. Stadler, Microwaves in Organic and Medicinal Chemistry, Wiley-VCH, Weinheim, 2005.

[70] R. Hoogenboom, U. S. Schubert, Macromol. Rapid Commun. 2007, 28, 368.

[71] C. Ebner, T. Bodner, F. Stelzer and F. Wiesbrock, Macromol. Rapid Commun. 2011, 32, 254.

[72] S. Barlow, S. R. Marder, Adv. Funct. Mater. 2003, 13, 517.

[73] D. Zemlyanov (2007), Introduction to X-ray Photoelectron Spectroscopy and to XPS Applications, http://nanohub.org/resources/2668.

[74] M. Gaft, R. Resfeld, and G. Panczer, Modern luminescence spectroscopy of minerals and materials. New York: Springer, 2005.

[75] D. V. Melnikov, J. R. Chelikowsky, Phys. Rev. Lett. 2004, 92.

046802.Y. Li, Y. Hu, Y. Zhao, G. Shi, L. Deng, Y. Hou, L. Qu, Adv. Mater. 2011, 23, 776.

[76] H. Song, S. Lee, Nanotechnology 2007, 18, 055402.

[77] L. Pang, Y. M. Shen, K. Tetz and Y. Fainman, Optics Express 2005, 13, No. 1.

[78] L. Biedermann, M. Bolen, M. Capano, D. Zemlyanov, R. Reifenberger, Phys. Rev. B 2009, 79, 125411.

[79] Z. Luo, Y. Lu, L. A. Somers, A. T. C. Johnson, J. Am. Chem. Soc. 2009, 131, 898–899.

[80] J. G. Zhou , C. Booker , R. Y. Li , X. T. Zhou , T. K. Sham , X. L. Sun , Z. F. Ding , J. Am. Chem. Soc. 2007, 129, 744.

[81] H. T. Li, X. D. He, Z. H. Kang, H. Huang; Y. Liu, J. L. Liu, S. Y. Lian, C. H. A. Tsang, X. B. Yang, S. T. Lee, Angew. Chem., Int. Ed. 2010, 49, 4430.

[82] G. Eda , Y. Y. Lin , C. Mattevi , H. Yamaguchi , H. A. Chen , I. S. Chen , C. W. Chen , M. Chhowalla , Adv. Mater. 2010, 22, 505.

[83] J. Y. Fan, P. K. Chu, Small 2010, 6, 2080.

[84] Z. Xie, F. Wang, C. Y. Liu, Adv. Mater. 2012, 24, 1716.

[85] Y. P. Sun, B. Zhou, Y. Lin, W. Wang, K. A. Fernando, P. Pathak, M. J. Mexiani, B. A. Harruff , X. Wang , H. Wang , P. G. Luo , H. Yang , M. E. Kose , B. Chen , L. M. Veca , S. Y. Xie , J. Am. Chem. Soc. 2006, 128, 7756.

[86] H. X. Zhao , L. Q. Liu , Z. D. Liu , Y. Wang , X. J. Zhao , C. Z. Huang , Chem. Commun. 2011, 47, 2604

[87] H. S. Chen, C. K. Hsu, H. Y. Hong, IEEE Photonics Tech Lett. 2006,

18, 193.

[88] W. S.Song, H. Yang, Appl. Phys. Lett. 2012, 100, 183104.

[89] E. Jang, S. Jun, H. Jang, J. Lim, B. Kim, Y. Kim, Adv. Mater. 2010, 22, 3076.

[90] J. Ziegler, S. Xu, E. Kucur, F. Meister, M. Batentschuk, F. Gindele, T. Nann, Adv. Mater. 2008, 20, 4068.

[91] Y. Q. Li, N. Hirosaki, R. J. Xie, T. Takeda, M. Mitomo, Chem. Mater. 2008, 20, 6704.

[92] J. K. Park, M. A. Lim, C. H. Kim, H. D. Park, J. T. Park, S. Y. Choi, App. Phys. Lett. 2003, 82, 683.

[93] H. S. Jang, H. Yang, S. W. Kim, J. Y. Han, S. G. Lee, D. Y. Jeon, Adv. Mater. 2008, 20, 2696.

[94] L. Ye, L. Z. Lai and J. Liu, IEEE Trans. Electron. Packag. Manuf., 1999, 22, 299.

[95] Y. Song, Y. Shen, H. Liu, Y. Lin, M. Li and C. W. Nan, J. Mater. Chem., 2012, 22, 8063.

[96] A. C. Balazs, T. Emrick and T. P. Russell, Science, 2006, 314, 1107.

[97] A. Haryono and W. H. Binder, Small, 2006, 2, 600.

[98] W. T. Kim, J. H. Jung, T. D. Kim and D.I. Son, Appl. Phys. Lett., 2010, 96, 253301.

[99] M. S. Mehata, M. Majumder, B. Mallik and N. Ohta, J. Phys. Chem. C, 2010, 114, 15594.

[100] M. Majumder, A. K. Chakraborty, B. Biswas, A. Chowdhury and B. Mallik, Synth. Met., 2011, 161, 1390.

[101] D. I. Son, D. H. Park, J. B. Kim, J. W. Choi, T. W. Kim, B. Angadi, Y.

Yi and W. K. Choi, J. Phys. Chem. C, 2011, 115, 2341.

[102] A. A. Syed and M. K. Dinesan, Talanta, 1991, 38, 815–837.

[103] A.G. MacDiarmid, Rev. Mod. Phys. 2001, 73, 701.

[104] Z. Z. Zhu, Z. Wang, H.L. Li, Appl. Surf. Sci., 2008, 254, 2934.

[105] T. Berzina, A. Pucci, G. Ruggeri, V. Erokhin and M. P. Fontana, Syn. Met. 2011, 161, 1408.

[106] B. Biswas, A. Chowdhury, B. Mallik, RSC Adv. 2013, 3, 3325.

[107] A. Sleiman, M. F. Mabrook, R. R. Nejm, A. Aayesh, A. A. Ghaferi, M. C. Petty, D. A. Zeze, J. Appl. Phys., 2012, 112, 024509.

[108] M. Rinkio, M. Y. Zavodchikova, P. Torma, A. Johansson, Phys. Status Solidi B, 2008, 245, 2315.

[109] C. Li, G. Hai-Ming, Z. Xi, D. Shi-Xuan, S. Dong-Xia, G. Hong-Jun, Chin. Phys. B, 2009, 18, 1622.

[110] S. L. Lim, N. J. Li, J. M. Lu, Q. D. Ling, C. X. Zhu, E. T. Kang, K. G. Neoh, ACS Appl. Mater. Interfaces, 2009, 1, 60.

[111] B. Biswas, A. K. Chakraborty, M. Majumder, A. Chowdhury. M. K. Sanyal, B. Mallik, Synth. Mat., 2012, 161, 2632.

[112] Q. D. Ling, S. L. Lim, Y. Song, C. X. Zhu, D. Siu-Hhung Chan, E. T. Kang, K. G. Neoh, Langmuir, 2007, 23, 312.

[113] C. M. Luk, L. B. Tang, W. F. Zhang, S. F. Yu, K. S. Teng, S. P. Lau, J. Mater. Chem., 2012, 22, 22378.

[114] L. B. Tang, R. B. Ji, X. K. Cao, J. Y. Lin, H. X. Jiang, X. M. Li, K. S. Teng, C. M. Luk, S.J. Zeng, J. H. Hao, S. P. Lau, ACS Nano, 2012, 6, 5120.

[115] Y. Mao, Y. Bao, L. Yan, G. Li, F. H. Li, D. X. Han, X. B. Zhang, L.

Niu, RSC Adv., 2013, 3, 5475.

[116] A. Ray, A. F. Richter, A. G. MacDiarmid, A. J. Epstein, Synth. Met., 1989, 29, 151.

[117] R. T. Morrison, R. N. Boyd, Electrophilic Aromatic Substitution in Organic Chemistry, 6th ed., Prentice Hall International, Inc., Upper Saddle River, NJ, 1992, pp. 517-546.

[118] M. L. Mueller, X. Yan, B. Dragnea, L. -s .Li, Nano Lett. 2011, 11, 56.

[119] J. Peng, W. Gao, B. K. Gupta, Z. Liu, R. Romero-Aburto, L. Ge, L. Song, L. B. Alemany, X. Zhan, G. Gao, S. A. Vithayathil, B. A. Kaipparettu, A. A. Marti, T. Hayashi, J.-J. Zhu, P. M. Ajayan, Nano Lett. 2012,12 (2), 844-849.

[120] S. J. Zhu, J. H. Zhang, C. Y. Qiao, S. J. Tang, Y. F. Li, W. J. Yuan, B. Li, L. Tian, F. Liu, R. Hu, et al., Chem. Commun. 2011, 47, 6858–6860.

[121] L. Ma, H. Hu, L. Y. Zhu, J. H. Wang, J. Phys. Chem. C, 2011, 115, 6195.

[122] K. P. Gong, F. Du, Z. H. Xia, M. Durstock, L. M. Dai, Science 2009, 323, 760.

[123] D. S. Yu, Q. Zhang, L. M. Dai, J. Am. Chem. Soc. 2010, 132, 15127.

[124] M. Deifallah, P. F. McMillan, F. J. Cora, Phys. Chem. C 2008, 112, 5447.

[125] Q. Li, S. Zhang, L. Dai, L.-S. Li, J. Am. Chem. Soc. 2012, 134, 18932–18935.

[126] M. Li, W. Wu, W. Ren, H.-M. Cheng, N.Tang, W. Zhong, Y. Du, Appl. Phys. Lett. 2012, 101, 103107.

[127] L. B. Tang, R. B. Ji, X. M. Li, K. S. Teng, S. P. Lau, J. Mater. Chem. C, 2013, 1, 4908.

[128] L. B. Tang, R. B. Ji, X. M. Li, G. X. Bai, C. P. Liu, J. H. Hao, J. Y. Lin, H. X. Jiang, K. S. Teng, Z. B. Yang, S. P. Lau, ACS Nano, 2014, 8(6), 6312-6320.

[129] L. B. Tang, R. B. Ji, X. M. Li, K. S. Teng, S. P. Lau, Part. Part. Syst. Charact. 2013, 30, 523-531.

[130] C. M. Luk, B. L. Chen, K. S. Teng, L. B. Tang, S. P. Lau, J. Mater. Chem. C, 2014, 2, 4526.

[131] D. Pan, J. Zhang, Z. Li, M. Wu, Adv. Mater. 2010, 22, 734.

[132] S. Zhuo, M. Shao, S. T. Lee, ACS Nano, 2012, 6 (2), 1059-1064.

[133] R. Hoffmann, J. Am. Chem. Soc., 90, 1968, 1475.

[134] L. Cao, X. Wang, M. J. Meziani, F. Lu, H. F. Wang, P. G. Luo, Y. Lin, B. A. Harruff, L. M. Veca, D. Murray, S. Y. Xie, Y. P. Sun, J. Am. Chem. Soc., 2007, 129, 11318-11319.

[135] C. Xu, W. W. Webb, J. Opt. Soc. Am. B 1996, 13, 481−491.